Earth's Isostatic and Dynamic Topography-A Critical Perspective

Alessandro M. Forte
Department of Geological Sciences
University of Florida
241 Williamson Hall
PO Box 112120
Gainesville, FL 32611-2120

And

David B. Rowley
Department of the Geophysical Sciences
The University of Chicago
5734 S. Ellis Ave.
Chicago, IL 60637

Key Points:

1) Earth's topography arises from the linear superposition of crustal isostatic and dynamic contributions
2) The global integral of dynamic topography that encompasses all non-crustal buoyancy sources equals zero
3) The best estimate of Earth's dynamic topography is the difference between observed and crustal isostatic topography

Abstract

Earth's topography arises from the linear superposition of isostatic and dynamic contributions. The isostatic contribution reflects the distribution of thickness and density of the crust overlying a static, non-convecting mantle. We argue that isostatic topography should be limited to the crust, thereby delimiting all sources for dynamic topography below the Moho. Dynamic topography is the component of the topography produced by normal stresses acting on the Moho that deflect the isostatic topography away from crustal isostatic equilibrium largely as a consequence of mantle flow dynamics. These normal stresses arise from pressure variations and vertical gradients of the radial flow in the convecting mantle. The best estimate of dynamic topography is from the residual topography, which is the difference between observed topography and crustal isostatic topography. Dynamic and residual topography are the same. It is clear that thermal anomalies horizontally advected by plate motions would not exist if the mantle were not convecting, therefore their contribution to topography is inherently dynamic in origin. The global integral of dynamic topography that encompasses all non-crustal buoyancy sources is demonstrated to be equal to zero. It follows that mantle convection cannot change the mean radius or mean elevation of the Earth. Since changes in ocean basin volume driven by changes in mean depth of the oceans are inherently part of dynamic topography, thereby requiring that continental elevations must also change, such that the global integral of these perturbations must also be equal to zero. This constraint has important implications for global long-term sea level and the stratigraphic record, among other features of the Earth system impacted by changes in Earth's dynamic topography.

Introduction

While it was postulated long ago that plate tectonics and mantle convection are intimately linked, the coupling between the two systems continues to generate active debate in the geosciences. Much effort has been invested to clarify the most important driving forces that maintain the observed plate motions, and their changes in time, and also to elucidate the coupling of the plates with the evolution of the mantle convective circulation. The ultimate goal is to develop physically consistent models of mantle convection that yield realistic predictions of long-term (>10^7yr) evolution of plate motions. A focus on horizontal motions is not complete, because plate tectonics is fundamentally a 3D process, in which the forces that drive tangential movement also drive radial displacements of the solid surface that change with time. This radial dimension of plate tectonics yields information on mantle convection dynamics that is distinct and complementary to that provided by observations of horizontal plate motions. In this contribution we primarily focus on this radial component of the convective dynamics and its role in Earth's topography.

Earth's topography is often discussed by distinguishing various components: (1) isostatic topography; (2) residual topography; and (3) dynamic topography (Forte, Peltier et al. 1993, Braun 2010, Flament, Gurnis et al. 2013, Steinberger 2016). Unfortunately, there are no agreed upon standard definitions of these components thereby leading to differences and some confusion even among the cognoscenti. For example, does the isostatic topography include only the crust and hence only reflect thickness and density variations above the Moho? In addition, what is the reference datum for computing crustal isostasy? Furthermore, if the definition of dynamic topography implies stripping out contributions related to oceanic depth-age, how is this justified given that this aspect of Earth's topography is clear evidence of mantle convection and plate tectonics (e.g. Forte et al. 1993)? If oceanic mantle lithosphere is included in the isostatic balance, is a square-root-age cooling or a plate model employed, and how are those dovetailed at continent-ocean boundaries? What constraints are used to model density anomalies in the mantle lithosphere under continents? If density perturbations in the continental mantle lithosphere are excluded from dynamic topography models, and these density anomalies change with time due to mantle convection, how can their contributions to topography not be dynamic? Dynamical coupling between subcontinental lithosphere and mantle convection can be appreciated, for example, by considering joint geodynamic and seismic tomographic modelling of hot mantle upwellings under Africa which show a correlation of lithospheric thinning or erosion with the upwellings (e.g. Fig. 5 in (Forte, Quéré et al. 2010). The spatiotemporal connections between changes in cratonic lithosphere and mantle plumes was recently emphasized in a joint analysis of African kimberlites and high-resolution tomographic images (Celli, Lebedev et al. 2020).

These are but a small number of questions that typically arise in discussions of Earth's topography and its change with time. The purpose of this assessment is to provide a critical perspective on these issues, based on our efforts over the past three decades to interpret and model Earth's variable topography. We acknowledge, at the outset, that this perspective will contrast with that presented in a number of recent treatments of dynamic topography. Our goal is to provide an in-depth quantitative discussion that addresses the questions cited above and, in the process, to elucidate a number of fundamental issues that have broad implications for understanding the mantle-dynamic origin of Earth's topography and its evolution over time.

A Fundamental Global Constraint on Dynamic Topography

Before engaging in a discussion of Earth's topography, it will be helpful to establish a fundamental constraint on the behavior of convective systems: the radial deflections of Earth's solid surface resulting from convection in the mantle do not change the mean radius and therefore mean elevation of the Earth. These radial deflections, or dynamic topography, which are a consequence of radial stresses that perturb the surface away from its hydrostatic equilibrium position, must therefore yield surface undulations whose global integral is zero. This zero-integral constraint is not new and it has been explicitly employed in a number of geodynamic modelling studies focusing on dynamic topography generated by buoyancy induced mantle flow (e.g. Forte et al. 1993, (Moucha, Forte et al. 2007), Conrad & Husson 2009, Steinberger, 2016). The geodynamic consequences of this global integral constraint are profound (e.g. Conrad & Husson 2009, Rowley 2017) and underlie much of the analysis presented in this paper. Although, as pointed out in Moucha et al. (2007), the basis of this global constraint derives from the principle of mass conservation, no explicit proof was presented. A proof of the zero-integral constraint on dynamic topography is still lacking in the published geodynamic literature. In the following we present a detailed proof of this constraint that is based primarily on the principle of mass conservation and, secondarily, on an understanding of the time-dependent relaxation of the free surface of a viscous fluid towards its equilibrium position.

The principle of mass conservation applied to a viscous compressible fluid is expressed by the following equation, where the anelastic approximation is assumed, which is valid when the Mach number is negligibly small and hence sound waves may be ignored (Jarvis and McKenzie 1980):

$$\vec{\nabla} \cdot (\rho\, \vec{u}) = 0 \quad , \tag{1}$$

where ρ and $\vec{u}$ are, respectively, the mass density and velocity of the fluid, $\vec{\nabla} \cdot$ is the divergence operator, and overscript arrows (here and in the following) denote vector quantities. Equation (1) shows that the mass flux $\rho\, \vec{u}$ is a solenoidal vector field that may therefore be expressed as follows (Backus 1958):

$$\rho\, \vec{u} = \vec{\nabla} \times \vec{\Lambda}\, p + \vec{\Lambda}\, q \quad , \tag{2}$$

where p and q are scalars that represent poloidal and toroidal mass flux, respectively, and $\vec{\Lambda} = \vec{r} \times \vec{\nabla}$, where $\vec{r}$ is the radial position vector. The first term on the right-hand side of equation (2) can be rewritten as:

$$\rho\, \vec{u} = \hat{r}\, \frac{\Lambda^2}{r} p + \hat{r} \times \vec{\Lambda} \left(\frac{1}{r} \frac{\partial\, rp}{\partial r} \right) + \vec{\Lambda}\, q \quad , \tag{3}$$

where $\hat{\mathrm{r}}$ is a unit radial vector and $\Lambda^2 = \vec{\Lambda} \cdot \vec{\Lambda}$ is the horizontal Laplacian operator. In equation (3), the operators $\hat{\mathrm{r}}$ x $\vec{\Lambda}$ ($= \vec{\nabla}_H$, the horizontal gradient on a unit-radius sphere) and $\vec{\Lambda}$ describe only the horizontal components of mass flux, whereas the radial component of mass flux ($f_r = \rho\, u_r$) is entirely described by:

$$f_r = \rho\, u_r = \frac{\Lambda^2}{r} p \ . \qquad (4)$$

Equation (4) implies that radial mass flux f_r must have a horizontal integral on any spherical surface S_r of radius r, concentric with the origin, that is identical to zero (Backus 1958). We can demonstrate this key property by using a spherical harmonic expansion of the poloidal mass flux scalar:

$$p(r, \theta, \varphi) = \sum_l \sum_m p_l^m(r)\, Y_l^m(\theta, \varphi) \ , \qquad (5)$$

where $Y_l^m(\theta, \varphi)$ is a spherical harmonic function of degree l and azimuthal order m that varies with latitude and longitude, (θ, φ), respectively, and $p_l^m(r)$ is the corresponding spherical harmonic coefficient that varies with radius r. Since $Y_l^m(\theta, \varphi)$ is an eigenfunction of the horizontal Laplace operator, such that $\Lambda^2 Y_l^m = -l(l+1)\, Y_l^m$, we can rewrite equation (4):

$$f_r(r, \theta, \varphi) = \sum_l \sum_m f_l^m(r)\, Y_l^m(\theta, \varphi), \text{ where } f_l^m(r) = -l(l+1)\, p_l^m(r) \ . \qquad (6)$$

From equation (6), we conclude that the degree $l = 0$ harmonic coefficient of the radial mass flux must be identical to zero, which necessarily implies that its global integral on any spherical surface of radius r in the mantle vanishes:

$$\oint_{S_r} f_r\, d^2S = \oint_{S_r} \rho\, u_r\, d^2S = 0 \ . \qquad (7)$$

We can now employ the mass-flux integral in equation (7) to derive a fundamental constraint on globally averaged dynamic topography generated by fluid motions in the mantle. We begin by considering a Gedanken-experiment in which, at reference time $t = 0$, a 3-D distribution of density anomalies is instantaneously placed in a hydrostatic fluid (mantle) in which all bounding surfaces are initially spherically symmetric (Fig. 1). Prior to this ($t < 0$), the density distribution $\rho = \rho_0(r)$ only varies with radius r. (In the work presented below, we employ the reference density $\rho_0(r)$ given by PREM (Dziewonski and Anderson 1981).

FIGURE 1- Here

Figure 1. A schematic cross-section through Earth's mantle, whose upper and lower bounding surfaces have mean radii r_0 and r_{CMB}, respectively, where the latter corresponds to the core-mantle boundary. a) Shows the configuration at time t=0, the instant when internal density perturbations are introduced and when the bounding surfaces are still spherically symmetric. b) At a slightly later time t >0, the transient mantle flow excited by these density perturbations displaces both bounding surfaces away from their initial positions and thereby creates 'dynamic topography' whose global integral is 0 (demonstrated in the main text). This transient flow ceases when the surface loads associated with the dynamic topography balance the loads generated by the internal density perturbations, where new local radii $r = r_e$ represent that balance.

We now consider, at a slightly later time $t > 0$, how the bounding surfaces are displaced away from their initial spherical position (Fig. 1b), in response to the short-term transient flow generated by the internal density anomalies $\delta\rho(r,\theta,\varphi)$, where the total density distribution is given by $\rho(r,\theta,\varphi) = \rho_0(r) + \delta\rho(r,\theta,\varphi)$. We now focus on the upper bounding surface, where the relationship between the time-dependent "growth" of surface topography and transient radial flow at the top of the mantle is:

$$u_{r_0}(\theta,\varphi,t) \equiv u_r(r_0,\theta,\varphi,t) = \frac{\partial}{\partial t} r(\theta,\varphi,t) \,, \tag{8}$$

where
$$r(\theta,\varphi,t) = r_0 + \delta r(\theta,\varphi,t) \tag{9}$$

and $\delta r(\theta,\varphi,t)$ is the dynamic topography generated by the transient displacement of the free surface away from its initial hydrostatic position at $r = r_0$. We note that at time $t = 0$, $\delta r(\theta,\varphi,t) = 0$, and that at time $t = t_e$, which is sufficiently long for the transient topographic undulations $\delta r(\theta,\varphi,t)$ to grow to their final equilibrium value, we have:

$$\delta r(\theta,\varphi,t_e) \equiv \delta r_e(\theta,\varphi) \text{ and } u_{r_0}(\theta,\varphi,t_e) = 0 \,, \tag{10}$$

This cessation of transient flow at time $t = t_e$ occurs when the surface loads associated with the equilibrium topography δr_e are in exact balance with (and opposed to) the loads associated with the internal density anomalies $\delta\rho$.

On the basis of expression (4), and using equations (8, 9), the radial mass flux associated with the transient growth of topography at the free upper surface is:

$$f_{r_0}(\theta,\varphi,t) = \rho(r_0,\theta,\varphi)\, u_{r_0}(\theta,\varphi,t) = \rho_0(r_0)[1+\varepsilon]\, \frac{\partial}{\partial t}\delta r(\theta,\varphi,t) \,, \tag{11}$$

where
$$\varepsilon = \delta\rho(r_0,\theta,\varphi)/\rho_0(r_0) \,. \tag{12}$$

On the basis of equation (11) and the constraint on the globally integrated radial mass flux in equation (7), which is valid at all times and at all radii in the fluid mantle, we find:

$$\oint_{S_{r_0}} \rho_0(r_0)[1+\ \varepsilon]\ \frac{\partial}{\partial t}\delta r(\theta,\varphi,t)\ \ d^2S = 0\ . \qquad (13)$$

We now integrate equation (13) between times $t = 0$ and $t =\ t_e$, and using (10), we obtain:

$$\oint_{S_{r_0}} \rho_0(r_0)[1+\ \varepsilon]\ \delta r_e(\theta,\varphi)\ \ d^2S = 0\ , \qquad (14)$$

where the integrand is the mass perturbation per unit area due to the growth of dynamic surface topography. Here we ignored the negligible time evolution of the density anomalies $\delta\rho$ during the short interval t_e required for the development of equilibrium topography (as justified below).

Equation (14) confirms that the total surface mass anomaly generated by the development of topography at the upper bounding surface is exactly equal to zero. Dividing by $\rho_0(r_0)$, we rewrite the surface integral in (14) as:

$$\oint_{S_{r_0}} [\delta r_e(\theta,\varphi) +\ \varepsilon\ \delta r_e(\theta,\varphi)]\ d^2S = 0\ . \qquad (15)$$

Since peak values of lateral density variations at the top of the mantle (e.g., in subducting lithosphere) are of order 1 to 2 %, then $\varepsilon \ll 1$ and we can accurately approximate the integral (15) by:

$$\boxed{\oint_{S_{r_0}} \delta r_e(\theta,\varphi)\ d^2S \doteq 0}\ . \qquad (16)$$

The equilibrium topography, δr_e, in expression (16) is called "dynamic topography" because it generates a surface load that is in balance with the integrated buoyancy forces arising from all density anomalies $\delta\rho$ in the convecting mantle. In equation (16), the global integral of dynamic topography over the surface of the Earth equals zero.

We note from expression (15), that the "error" in constraint (16) is contained in a second-error perturbation ϵ^2 :

$$\epsilon^2 = \oint_{S_{r_0}} [\varepsilon\ \delta r_e(\theta,\varphi)]\ d^2S\ . \qquad (17)$$

In mantle convection modelling, such second-order perturbations are generally treated as negligible and hence are ignored. We confirm this by evaluating ϵ^2 using mantle density anomalies and corresponding dynamic surface topography predicted using the *GyPSuM* tomography model (Simmons, Forte et al. 2010). The values of ε range from -0.6% to 0.5% and δr_e ranges from -1957 m to 2967 m. The peak values of $\varepsilon\, \delta r_e$ thus range from -13 m to 5 m and its global integral, defined in (17), is $\epsilon^2 = -0.7$ m. We may alternatively evaluate the magnitude of ϵ^2 using an *a-priori* subducted slab model, employed by Lu et al. (Lu, Forte et al. 2020), which is based on the thermal modelling of Stadler et al. (Stadler, Gurnis et al. 2010). In this case, employing a spherical harmonic expansion of slab density anomalies truncated at degree $l = 128$, the peak positive value of ε is 2.3% while δr_e ranges from -2168 m to 119 m, and we find that $\epsilon^2 = -0.2$ m. It is therefore clear that ϵ^2 is negligibly small and the global integral constraint (16) applies with high accuracy.

Above, we noted that the dynamic topography is in equilibrium with the internal density loads after the surface boundary relaxes over a "sufficiently long" time interval t_e, which is also assumed to be short relative to the time scale over which internal density anomalies evolve as a consequence of thermal convection. It is therefore important to quantify the magnitude of t_e in relation to the time scale relevant to mantle convection dynamics. The viscous relaxation of the surface boundary, in response to transient flow generated by internal density anomalies, is exactly analogous to the glacial isostatic adjustment (GIA) of the mantle in response to changing surface ice and water loads. As in GIA problems (e.g. (Peltier 1974); see also (Richards and Hager 1984), the topographic undulations generated by the viscous relaxation of the solid surface are mathematically described by a spherical harmonic expansion:

$$\delta r(\theta,\varphi,t) = \sum_l \sum_m \delta r_l^m(t)\; Y_l^m(\theta,\varphi) \quad , \tag{18}$$

where each harmonic coefficient, corresponding to topographic contributions of different horizontal wavelengths defined by the degree l, has a multi-modal time dependence expressed by:

$$\delta r_l^m(t) = \sum_{n=1}^{N} r_{ln}^m \left[1 - e^{-t/\tau_{ln}}\right] , \tag{19}$$

where the N modes arise from discontinuous changes (e.g. at the surface, base of crust, core-mantle boundary) in the reference density structure $\rho_0(r)$. The time dependence in (19) applies to the Heaviside loading history depicted in Fig. 1. Each mode (indicated by the index n in equation 19) is characterized by a relaxation, or viscous decay, time τ_{ln} whose value depends on the horizontal wavelength (given by degree l) and viscosity structure of the mantle, and an amplitude r_{ln}^m that depends on the integrated density anomalies $\delta\rho$ in the mantle. The relaxation of the free surface and corresponding growth of topography, described by equations (18-19), requires transient flow in the viscous mantle. The radial component of this transient flow at the upper bounding surface is:

$$u_{r_0}(\theta, \varphi, t) = \frac{\partial}{\partial t}\delta r(\theta, \varphi, t) = \sum_l \sum_m \sum_{n=1}^{N} \left[\left(\frac{r_{ln}^m}{\tau_{ln}}\right) e^{-\,t/\tau_{ln}}\right] Y_l^m(\theta, \varphi)\ . \quad (20)$$

From the prescription for the equilibrium time t_e in expression (10), it is clear from equation (20) that transient mantle flow implicated in the growth of surface topography decays to negligible values when $t = t_e$ is about three times greater than the longest viscous decay time: $t_e \cong 3 \times \max(\tau_{ln})$. The longest wavelength-dependent decay times predicted on the basis of current geodynamically constrained radial viscosity profiles are about $\sim 20\ ka$ (Forte, Moucha et al. 2010), and therefore $t_e \cong 60\ ka$. This time interval for the development of equilibrium surface topography is much shorter than the characteristic time scale for the evolution of density anomalies in the convecting mantle, which is of order $\sim 1\ Ma$. This separation of time scales implies that the evolution of dynamic topography at Earth's surface, in response to time-dependent variations of density anomalies in the convecting mantle, may at all times be considered to be in nearly complete equilibrium with the buoyancy forces acting on Earth's upper bounding surface.

Equation (16) demonstrates that the integral of dynamic topography over the surface of the Earth must vanish. Thus, the mean (i.e. global horizontal average) of dynamic topography and the change in dynamic topography is zero at all times. Importantly, this constraint pertains to dynamic topography produced by all density anomalies in the mantle including, for example, the age-dependent subsidence of the cooling oceanic lithosphere. Although mantle convection cannot give rise to changes in the mean radius of the Earth, at any instant in time, on very long time-scales where secular cooling is important ($\Delta t \gg 100\ Ma$), the Earth's mean radius (r_0) does shrink. Following (Jaupart, Labrosse et al. 2007) and equation (A23) in Appendix A:

$$\Delta r_0 \approx r_0 \frac{\langle\alpha\rangle}{3} \Delta T \left(1 + \varepsilon \frac{16\pi}{45}\right), \quad (21)$$

Where Δr_0 is the change in mean radius, $\langle\alpha\rangle$ is the average thermal expansion coefficient, generally estimated to be between 1 and $2 \times 10^{-5}\ K^{-1}$ (Jaupart, Labrosse et al. 2007), ΔT is the change in bulk average temperature, and $\varepsilon = {K_s}^{-1} G\, \rho_0^2\ r_0^2 \approx 0.33$ is a parameter (see Appendix A) that quantifies the impact of compressibility (${K_s}^{-1}$) on the contraction. Petrological data and some thermal evolution models (e.g. (Herzberg, Condie et al. 2010) suggest that over the past 2.5 to 3.0 Ga, the average rates of change of bulk temperature, $\Delta T/\Delta t$, range between -50 *K*/Ga to -100 *K*/Ga. The secular cooling rate is likely to have changed with time and may therefore differ from these estimates of long-term average rates (e.g. (Korenaga 2008)). Assuming $\langle\alpha\rangle \approx 2 \times 10^{-5}\ K^{-1}$, equation (21) then yields estimated average rates of thermal contraction, $\Delta r_0/\Delta t$, that range between -2.7 to $-5.5 \times 10^{-4}\ cm/yr$, which is 4 orders of magnitude smaller than typical mantle convective flow velocities and transient topography changes due to viscous relaxation. We finally estimate that Earth's mean radius has contracted between 270 to 550 *m* over the past 100 Ma (i.e. since the mid-Cretaceous), and between 8 to 16 *km* over the past 3 Ga. It should be understood that the zero-integral dynamic topography constraint (eq. 16) applies at each instant during the long-term secular contraction of Earth's mean radius, and, as discussed below, the change in mean radius is unidirectional and not expanding then contracting on these time-scales, as implied by some models (e.g. Müller et al. 2008).

We conclude this discussion by underlining the key result in equation (16): on a thermally convecting mantle, the mean value of dynamic topography variations is zero. As will be discussed below, this zero integral constraint has important consequences for understanding the link between changes, for example, in mean depth of the oceans due to variations in mean ocean floor age and continental flooding as discussed by Rowley (2017) for a simple "Pitman-type" world. (i.e. (Pitman 1978).

Our Perspective: Simple Definitions of the Components of Earth's Topography

The focus of this paper is to review current understanding of Earth's large-scale topography. Here large-scale refers to lengths greater than the flexural wavelength of the lithosphere (i.e. >100's km). On geological time scales ($\geq\ \sim 1MY$), Earth's topography may be regarded as the (linear) superposition of two distinct contributions (Forte, Peltier et al. 1993): (i) crustal isostatic topography, generated by heterogeneities in crustal thickness and density; (ii) dynamic topography, due to radial deflections of the solid surface in response to normal stresses generated by buoyancy forces arising from all density anomalies in the mantle. Within this framework, "residual topography", which is the difference between the observed topography and crustal isostatic topography, is synonymous with dynamic topography. In other words, residual topography is the component of the observed topography that requires explanation largely, if not entirely, from mantle sources. We will return to the caveat of "largely" in the preceding sentence when we discuss uncertainties in the current understanding of crustal thickness and density distribution and the resulting impact on estimates of the residual topography.

We will use as our reference observed topography, a radially adjusted version of the *Etopo1_Ice* digital elevation model (Amante and Eakins 2009) that is used in the *Crust1.0* crustal heterogeneity model (Laske, Masters et al. 2013), in which the radial adjustment removes all effects of glacial isostatic adjustment (GIA) due to past glacial ice loading, using the full sea level modelling (Fig. 2a) (Raymo, Mitrovica et al. 2011). This reference topography thus removes the effects of Pleistocene to recent glacial isostatic adjustment (GIA) that currently contaminates Earth's topography, while preserving the current surface ice as included in the *Crust1.0* model. The global integral of the GIA topography correction is zero, so that the mean elevation of the adjusted topography is identical with the starting *Etopo1_Ice* model, which has a global mean elevation of -2384.6 m. Because crustal model *Crust1.0* has a spatial resolution of 1 arcdegree we employ a corresponding 1 arcdegree-average GIA corrected topography (Fig. 2b) for the discussions below.

FIGURE 2 Here

Figure 2. (a) One arcdegree correction to remove the remaining GIA resulting from past changes in ice loading using the full solution of the sea level equation (Raymo, Mitrovica et al. 2011). (b) One arcdegree gridded topography derived from Etopo1_Ice with including radial correction to remove the effects of all remaining glacial isostatic adjustments due to Pleistocene glaciations. Plate boundaries from Bird (Bird 2003).

Crustal Isostatic Topography

The first and most important source of topography, the crustal system, can be readily modelled using classical isostasy theory, derived from Archimedes principle, provided the thickness and density of each crustal column is known. It is critically important that the predicates of isostasy are fully appreciated. In this modelling, the crust "floats" on a **hydrostatic** underlying mantle in which there are **no dynamical forces** (i.e. **the mantle is not convecting**). In addition to the crust, *sensu stricto*, there may be sediments, ice or water on top of the crust that contribute to the crustal loading and these need to be included in the isostatic calculation. Any process that alters crustal thickness, such as shortening or extension due to tectonics, or erosion or deposition associated with sediment production and redistribution, will change the isostatic height of the crust, but otherwise an unchanging crustal column maintains a constant isostatic height with time.

The definition of isostatic topography presented above provides a simple conceptual framework that we quantify in the following. The classical method for calculating isostatic crustal topography employed, for example, by Forte et al. (Forte, Peltier et al. 1993, Forte, Simmons et al. 2015) is presented in algorithmic form for a multi-layer crust by (Pari and Peltier 2000). This framework treats crustal isostasy in terms of perturbations of crustal loads acting on an undulating Mohorovičić discontinuity: the "Moho", defining the boundary between the crust and the mantle. Within this framework, the deflection of the Moho due to crustal loading is computed such that the total pressure acting at a fixed reference depth below the crust, in the (lithospheric) mantle, is constant at all locations thereby ensuring the hydrostatic equilibrium of the underlying mantle. This condition requires that the total pressure perturbation, δP_{total}, relative to the global (horizontally averaged) mean pressure, must equal zero at all geographic locations. The latter requirement yields the following constraint on the local displacement of the radial position of the Moho, δr_{moho}:

$$\delta P_{total} = \{ \rho_{moho} \, \delta r_{moho} + \sigma_{crust} - \overline{\sigma_{crust}} \} \, g = 0 \, , \qquad (22)$$

where,

$$\sigma_{crust} = \sum_{i=1}^{N} \rho_i \, h_i \, , \qquad (23)$$

and g is the gravitational acceleration, ρ_{moho} is the density of the mantle below the Moho, ρ_i and h_i are the density and thickness, respectively, of each layer in an N-layer crustal model, σ_{crust} is the total mass per unit area of each crustal column, and $\overline{\sigma_{crust}}$ is the global (horizontally averaged) mean crustal mass per unit area. The summation in (23) also includes sediment, water and/or ice layers that may overlie the solid basement rocks in each crustal column. We note that the term $(\sigma_{crust} - \overline{\sigma_{crust}}) \, g$ in expression (22) is the perturbed load (having units of pressure) of each crustal column relative to the global mean load. Expression (22) finally yields the following equation for the isostatic radial displacement of the Moho:

$$\delta r_{moho} = (\overline{\sigma_{crust}} - \sigma_{crust}) \, / \, \rho_{moho} \, . \qquad (24)$$

We use the sub-Moho density $\rho_{moho} = 3380.76 \text{ kg/m}^3$, as specified in the *PREM* reference Earth model (Dziewonski and Anderson 1981), which is spherically symmetric (i.e. laterally homogeneous) and upon which a laterally heterogeneous crustal model such as *Crust1.0* (Laske, Masters et al. 2013) is draped. In the more recent 1-D reference Earth model, *STW105* (Kustowski, Ekstrom et al. 2008), $\rho_{moho} = 3289.84 \text{ kg/m}^3$. We note from expression (24) that the global mean of the Moho deflections generated by laterally variable crustal loads is identically equal to zero.

The local radial displacement, δr_1, of the external surface (i.e. layer 1 in expression 23) relative to its mean radius is given by:

$$\delta r_1 = \left(h_{crust} - \overline{h_{crust}} \right) + \delta r_{moho} \, , \text{ where } h_{crust} = \sum_{i=1}^{N} h_i \, , \qquad (25)$$

and $\overline{h_{crust}}$ is the global (horizontally averaged) mean thickness of an N-layer representation of the crust. In equation (25) the summation includes water or ice layers. In particular, for the *CRUST1.0* model (Laske, Masters et al. 2013), layers 1 and 2 correspond to water and ice, respectively. In the *PREM* reference Earth model, the radius r_1 (= 6371 km) also corresponds to the surface of the globally defined water layer. We note that expression (25) implies that the (horizontally averaged) mean value of the local radial displacements of the external surface, δr_1, is identically equal to zero and hence the mean radius of the external surface is maintained and equal to that of the reference Earth model.

Finally, the isostatic radial deflection of the solid surface of the crust, δr_{surf}, which underlies the outer water layer is given by,

$$\delta r_{surf} = \delta r_1 - h_1 \, , \tag{26}$$

where h_1 is the thicknesses of the water in each crustal column. We replace the water thickness originally specified in the *Crust1.0* model with the GIA-corrected values, ensuring that the top of each water column corresponds to the geoid (approximated here as a spherical surface) and that the total water volume is conserved. This calculation therefore requires an iterative solution of the sea level equation, as in Austermann & Mitrovica (Austermann and Mitrovica 2015), in which shorelines are allowed to migrate until consistency is achieved. The global variation of crustal isostatic topography we thus obtain from expressions (24 – 26) is presented in Figure 3. Since the global mean value of δr_1 is equal to zero, it is clear from eq. (26) that the global mean value of the isostatic topography of Earth's solid surface is determined by the global mean depth of the water layer: $\overline{\delta r_{surf}} = -\overline{h_1} = -2619.4$ m that should equal the mean elevation of the surface of -2384.6 m , but does not for reasons touched on below. Similarly, the observed 1-arcdegree gridded topography derived from *Etopo1_Ice* (Fig. 2) must accommodate the same volume of water in the *Crust1.0* model, hence (following eq. 26) it must also have a mean solid surface radius that is identical to the isostatic topography.

Figure 3 Here

Figure 3. Crustal isostatic topography determined from Crust1.0. This calculation conserves the total volume of water while ensuring the water surface corresponds to the geoid. Mean elevation of the isostatic topography is -2384.6 m.

There are certain subtleties in the preceding treatment that are worth emphasizing. The most important concerns the variation in water depth overlying the oceanic crust. The depth of the ocean layer in crustal models, such as CRUST1.0, is variable and it increases according to the age of the ocean lithosphere. This age-dependent ocean depth and hence water-load has been included in past modelling of isostatic crustal topography (e.g. Pari and Peltier 2000, Forte et al. 2015) completely independent of any particular depth-age model. This variability in ocean depth is, however, a manifestation of mantle dynamics in which the thermal evolution of the oceanic lithosphere, which is the upper thermal boundary layer of the convecting mantle, controls the subsidence of the oceanic crust. Since crustal isostasy assumes a completely hydrostatic and hence non-convecting mantle, it can be argued that an internally consistent model of isostatic topography requires that the age-dependent variability of ocean depth should be rectified. To this end, as described above, we begin with an air-loaded crustal isostatic topography to which we progressively add the water load, until the volume of water equals the volume of liquid water on Earth ($\sim 1.33 \times 10^9\ km^3$) and the water surface follows a geoid (Figure 3). This adjustment has a significant impact on the resulting crustal isostatic topography relative to one that includes imposed (ocean-age-dependent) water load variations, characterized by a difference of about ±1.1 km relative to the isostatic topography as derived from *Crust1.0* (Figure 4). Recalling that crustal isostasy is relative to a non-convecting mantle and thus reflects only contributions from crustal thickness and crustal density alone, this model of the crustal isostatic topography, shown in Figure 3, is the most internally consistent result and is characterized by a flat-bottomed ocean. Although the global isostatic topography is not explicitly shown in Steinberger (2016), his modelling of Crust1.0 non-isostatic topography implies an isostatic oceanic bathymetry that is also flat-bottomed.

Figure 4 Here

Figure 4. Difference between crustal isostatic topography from Crust1.0 with variable (ocean-age-dependent) water-loading of the oceanic lithosphere and the internally consistent calculation shown in Fig. 3.

Another subtlety concerns the representation of oceanic crustal structure in *Crust1.0* (Laske, Masters et al. 2013), whose thickness and density is quite homogeneous. *Crust1.0* oceanic crustal thickness, for grid ages less than 170 Ma, ranges from 2.3 to 35.8 km with a mean of 7.4±2.1 km (1σ). The mean density of the oceanic crust is 2952±22 kg/m^3 (1σ). The relatively narrow range of the majority of oceanic crustal properties in *Crust1.0* leads to a small range in isostatic depths. There are variations in the thickness and density of overlying oceanic sediments that yield some variation in isostatic depth. However, in the *Crust1.0* model, the densities specified for very young oceanic crust (i.e. $age < 4\ Ma$; although a few smaller backarc basins, with ages as old as 29 Ma, are also included) are decreased by a few hundreds of kilograms per cubic meter in each of the three crustal layers. These density reductions contribute to increased isostatic topography of ridges relative to older oceanic crust of up to 471 m. The basis for these reduced oceanic crustal densities is not clear, nor whether their effect should be included in the calculation of isostatic topography as they are in Fig. 3.

Another issue worth noting is that there are detailed aspects of currently employed 1-D reference Earth models that mismatch the global Crust1.0 model that we employ. In both *PREM* (Dziewonski and Anderson 1981) and *STW105* (Kustowski, Ekstrom et al. 2008), the spherical, global ocean layer is 3 km thick, implying a water volume of $1.52 \times 10^9\ km^3$ whereas the actual volume of water, including the water equivalent of all grounded ice, occupies a volume ($\sim 1.36 \times 10^9\ km^3$) that corresponds to a global-mean ocean depth of about 2.661 km. If present-day grounded ice is retained (i.e. not converted to water) in the crustal model, the ocean volume is $\sim 1.33 \times 10^9\ km^3$ yielding a global ocean whose depth is 2.613 km. The mean elevation of the solid surface in both *PREM* and *STW105* is -3000 m, whereas the mean elevation in *Etopo1_Ice* is -2384.6 m. The 228-metre difference between the mean (isostatic) depth of -2613 m and (observed) -2385 m arises from a fundamental distinction between the mean radius of the Earth as specified by *PREM* (and *STW105*) and the mean radius determined on the basis of Earth's actual topography. A sphere whose volume is the same as that of the reference ellipsoid that best fits Earth's geoidal surface is used to determine the mean Earth radius in *PREM*, which is 6371.0008 km, based on the reference ellipsoid in the 1980 *World Geodetic System* (Moritz 2000). However, the geoidal surface, and hence the reference ellipsoid, does not include the additional continental topography above the geoid (i.e. above sea level). This continental topography, as represented in the 1-arcdegree averaged *Etopo1_Ice* model, yields an additional mean elevation of 228 m relative to the mean Earth radius in *PREM*. A more detailed discussion of this issue may be found in (Chambat and Valette 2001).

Finally, both *PREM* and *STW105* specify an upper crustal layer with a density of 2600 kg/m^3 that is 12.0 km thick and lower crust of 2900 kg/m^3 with thickness of 9.4 km, yielding a total crustal thickness of 21.4 km with mean density of 2732 kg/m^3. In contrast, *Crust1.0* (Laske, Masters et al. 2013) has a mean crustal thickness, including sediments, but excluding water and ice, of 19.0 km with a mean density of 2823 kg/m^3. In summary, current 1-D reference Earth models have 11.0% more water than present on Earth's surface, 8.3% more crustal mass than accounted for by *Crust1.0*, and has a mean radius that is 228 m less than Earth's mean radius.

Figure 5 (red lines) shows the starting GIA-corrected *Crust1.0* cumulative and differential hypsometry that represents the observed topography. The corresponding crustal isostatic topography as represented by the cumulative (black line) and differential hypsometry (blue line) are also shown. Earth's bimodality is clearly reflected in the differential hypsometries, but there is a switch from GIA-corrected hypsometry with a dominant shallow mode, as is true of the uncorrected hypsometry (Rowley 2013), to the crustal isostatic topography where the deep oceans represent the dominant mode. As shown, oceanic crustal regions are essentially flat in the crustal isostatic hypsometry whereas there is a persistent slope in the observed hypsometry. This reflects the fact that the oceanic crust is, to first order, homogeneous in thickness and density and thus would be expected to stand at essentially constant elevation as shown by the blue curve. A second order contributor to this is the absence of variations in oceanic crustal thickness in regions of many oceanic plateaus and hotspot tracks in the *Crust1.0* dataset. The persistent slope in the observed topography reflects convection-related dynamic topography of the oceanic lithosphere depth-age relationship.

Figure 5 Here

Figure 5. Cumulative hypsometry of the crustal isostatic topography of Crust1.0 relative to PREM with a mean elevation is -2384.6m (black). Differential hypsometry of the crustal isostatic topography is shown along the left axis by the blue line relative to the scale at the bottom left. Sea level is computed as the volume of the topography equivalent to the volume of the water at the surface of the Earth. Sea level relative to this hypsometry would be at -640m. GIA-corrected cumulative and differential hypsometry (red) of Crust1.0 topography with differential hypsometry scale in the lower right. Sea level of the GIA-corrected topography is -5 m. Note the factor of 4 difference in the differential hypsometry scales.

As noted above in our discussion of Fig. 3, we compute sea level on the isostatic topography via 2-D integration of the volume of water to the geoid incorporating shoreline migration. This yields a height of sea level relative to the isostatic topography of -640 m. A primary difference between our approach and that of Steinberger (2016) is that we constrain the resulting solution by the volume of water in the oceans, hence limit water-loading only to those depths below the geoid. In contrast, Steinberger (2016) applies a water load correction to all regions currently below 0m elevation requiring approximately 15% more water than exists at the surface of the Earth, as should be clear from Fig. 5. This implied additional water increases the water-load, thereby deepening the mean depth of the oceans relative to Fig. 5.

In contrast to the oceans being deeper, the isostatically supported continents stand high, in fact, considerably higher than the average elevation of the continents today (Figure 5). The mean isostatic elevation of the oceanic region (i.e. heights below 0m) is -4553m, whereas the continents (i.e. heights above 0m) have a mean isostatic elevation of 1928m. These values contrast with -3707m and 786m, respectively, in the GIA corrected *Crust1.0* topography with a corresponding "sea level" height of -4.9m at 1 arcdegree resolution. These differences clearly demonstrate the role of non-isostatic (i.e. dynamic) topography in controlling ocean basin volume and continent elevation.

It is instructive to explore to what extent Earth's present-day continental topography departs from crustal isostatic equilibrium by considering the magnitude of changes to crustal structure that would yield hydrostatic conditions in the underlying mantle, as expressed in equation (22). To this end, we consider what perturbations to the crustal structure described by the *Crust1.0* model would be required to establish an equality between the isostatic and observed topography and whether these changes are large compared to likely uncertainties in the model itself. We start with the understanding that oceanic topography is dominated by sub-moho processes and therefore perturbing crustal thickness or density to bring oceanic topography into equilibrium is not meaningful. As a result, this exercise focuses entirely on the regions above sea level. For this exercise we estimate end member solutions. One end member involves iteratively adjusting each column crustal thickness, while assuming the mean crustal column density is correct, until the load of each column (i.e. total pressure) at the depth of the compensation is the same (Fig. 6a). As anticipated from consideration of Fig. 5, the thickness of continental crust must decrease, on average, to bring the isostatic topography into equilibrium with observed topography. More precisely, the mean decrease in crustal thickness for regions above sea level is 10.2 km from a mean of 39.1 km, where local perturbations range from +35.8 to -21.5 km. Framed in terms of percent change in thickness of regions above sea level, the mean change required is -24.6% with 95% of changes between -43.1% and +2.9%. The other end member involves iteratively adjusting the mean column density, assuming the crustal thickness is correct (Fig. 6b). The average change in mean crustal density, including ice, of continental regions is 148.3 kg/m^3 from a mean of 2790.7 to 2939.0 kg/m^3, where local perturbations range from -619.8 to 347.3 kg/m^3. These required perturbations to column density represent a mean increase of 5.3% with a 95% range from -0.6 to 9.9% change. Although *Crust1.0* does not specify uncertainties in either crustal thickness or density, the required changes in crustal thickness are large relative to other estimates of uncertainty in crustal thickness (Szwillus, Afonso et al. 2019). It is therefore unlikely that departures of observed topography from isostasy can be explained solely in terms of errors in crustal thickness. Similarly, the density changes required are pretty large, however, it is less clear that *in-situ* crustal densities (particularly in the deep crust) are sufficiently well constrained to preclude accounting for some fraction of the resulting non-isostatic (i.e. residual) topography. In this regard, it is worth noting that the density of continental lower crust would have to increase by more than 10% to achieve a 1-km reduction of elevation in continental regions (Pari and Peltier 2000) and thereby shift the isostatic topography of continents closer to observed values (Fig. 5)

Figure 6 Here

Figure 6. Perturbations to Crust1.0 (a) crustal thickness and (b) mean crustal density of regions above sea level, such that the isostatic topography equals observed topography.

Dynamic Topography

The second source of topography, the dynamic topography, arises from buoyancy forces generated by convective circulation in the mantle, which includes density variations in the mantle lithosphere due to thermal and petrological heterogeneity. The <u>buoyancy forces associated with mantle convection are generated by lateral temperature and petrologic variations</u> associated with hot mantle upwellings (e.g.

plumes) and cold mantle downwellings (e.g. subducted oceanic lithosphere) that together drive the mantle-wide flow. Shallow-mantle buoyancy variations also arise from advected density anomalies in the asthenosphere or through changes in lithospheric mantle composition or from deformation of the lithospheric mantle layer due, for example, to plume-induced thinning, or alternatively to thickening which may lead to partial or complete removal of the mantle lithosphere (e.g. "drips" or delamination). This shallow deformation is a dynamical process that is generated by temperature anomalies and viscous stresses arising from the sublithospheric, mantle-wide convective flow.

All processes that alter the buoyancy distribution in the mantle, including the lithospheric mantle, will alter the dynamic topography and hence total (observable) topography of the Earth. Estimates of the relative importance of "shallow" versus "deep" mantle contributions to dynamic topography suggest that about 50% of the dynamic topography is produced by buoyancy in the top 200 km of the mantle, and the remaining 50% is due to buoyancy distributed at all depths below 200 km (Forte 2007). As stated above, a direct constraint on dynamic topography, shown in Figure 7 and henceforth denoted "FR2021", is obtained by subtracting the crustal isostatic topography (Figure 3) from the observed or in our case GIA-corrected topography (Figure 2). This component has also been referred to as "residual topography", as it is the topography that requires explanation from buoyancy, largely, if not entirely, residing in the mantle.

Figure 7 Here

Figure 7. Dynamic topography of the Earth calculated as the difference between the observed topography (Figure 2b) and the crustal isostatic topography (Figure 3). Note that since Crust1.0 does not account for variations in crustal thickness of various aseismic ridges (e.g. 90°E, Walvis, Rio Grande, Hawaiian chain, among others), their crustal isostatic topography is not represented and so they are masked by outlines of LIPS from (Coffin and Eldholm 1994) in gray.

We adopt this conceptual formulation of topography, as originally proposed by (Forte, Peltier et al. 1993, Forte, Peltier et al. 1993), for two simple reasons: First and foremost is that the integral of dynamic topography over the surface of the Earth, as defined in this way, is zero, as is the global integral of dynamic topography change as a function of time (see eq. 16). This global integral constraint is thus critical in that it provides a framework for understanding how changes in dynamic topography must be accommodated globally. A simple consequence of this global integral property is that the crustal isostatic topography, GIA-corrected topography, and present topography (corrected for the small difference between mean radius of PREM and that of the Earth) all share the same mean elevation of the solid surface, because all of the corresponding perturbation fields also have global integrals equal to zero.

The second reason is that past subdivisions of contributions to residual topography into sub-sources such as, thermal cooling of the oceanic lithosphere, compositional variations in the upper mantle such as between cratons and oceans or between continental areas with and without cratonic roots, treat such sources as if they themselves do not reflect or directly relate to mantle dynamics. When parsed in this way, it is unlikely that topography contributions from these individual buoyancy sources, when integrated globally, yield a mean topography perturbation that equals zero. Thus, for example, the elevation of the oceanic lithosphere at the ridges represents a large positive contribution to overall non-isostatic topography of the Earth resulting from shallow upper-mantle buoyancy variations (Figures 7). Treated independently, this component does not appear to need balancing by other contributions to dynamic topography. In fact, in past treatments of long-term sea level change (Müller, Sdrolias et al. 2008, Conrad and Husson 2009, Spasojevic and Gurnis 2012), this component is treated independently without balancing contributions (e.g. under continents) thus implying increases and decreases in mean radius of the Earth over the past ~140 Myr (Müller, Sdrolias et al. 2008) to 230 Myr (Wright, Seton et al. 2020) as highlighted by (Rowley et al., submitted).

From our perspective, this approach to understanding the observed topography as the simple linear superposition of crustal isostatic topography and dynamic (or residual) topography provides the simplest and clearest way to think about this problem. The observed topography, with or without GIA corrections, is well known, although direct measurements of oceanic depths remain relatively poorly observed (e.g. (Weatherall, Marks et al. 2015). Global crustal thickness models are presumably improving with time as a result of increasing numbers of approaches that image and resolve the depth to the Moho (Szwillus, Afonso et al. 2019). Improved constraints on crustal density are also needed to reduce uncertainty in the crustal isostatic topography. The unexplained part of the observed topography, i.e. the residual topography, then becomes the focus where other observational geophysical constraints (including seismology and seismic tomography, free-air gravity, and mantle flow calculations) help to bound models that account for this dynamical component of the topography (see Forte et al. 2015).

It is not our intent here to review the approach of (Forte 2007, Forte, Simmons et al. 2015) that has been used in development of tomography models (Simmons, Forte et al. 2006, Simmons, Forte et al. 2009, Simmons, Forte et al. 2010, Lu, Forte et al. 2020, Glišović, Grand et al. 2022) of the volumetric heterogeneity in seismic velocity and density throughout the mantle, including both continental and oceanic lithospheric mantle. These joint seismic-geodynamic tomography models provide optimal fits to plate motions, dynamic=residual topography (Figure 7), free-air gravity, excess ellipticity of the CMB, and incorporate mineral physics to constrain the 3-D density distribution of the mantle, including the mantle lithosphere. This globally coherent approach treats dynamic topography as the integrated consequence of all sources of buoyancy operating within the complex viscosity structure of the mantle, rather than parsing individual components such as continental mantle lithosphere, oceanic mantle lithosphere, asthenospheric and transition zone, and lower mantle contributors to the dynamic topography. From this perspective, they are all interconnected components of Earth's mantle convective system.

Other Perspectives on Isostatic, Residual, and Dynamic Topography

There has been considerable discussion and outstanding differences in the published literature concerning definitions of isostatic, residual, and dynamic topography, which have led to confusion and has required (even experienced) readers to carefully parse how each publication defines and treats these terms. This is an unfortunate situation, therefore in the following review we will adhere to the definitions we presented above and highlight important distinctions with how others have used these same terms.

Continental Regions- Isostatic Topography

It is perhaps remarkable that differing approaches or definitions have been employed for estimating the isostatic contribution to Earth's topography. Some differences simply originate in the use of different crustal models, including *Crust2.0* (igppweb.ucsd.edu/~gabi/crust2.html, Forte 2007; Steinberger, 2007), or *Crust5.1* (Mooney, Laske et al. 1998, Pari and Peltier 2000), or simple continent-ocean crust (Forte et al. 1993a), but are otherwise conceptually equivalent. The closest comparison is with the Steinberger (2016) models of isostasy, henceforth 'Sb2016' for brevity, because he provides an explicit discussion of each component incorporated within his topography model, and thus it is possible to replicate his results allowing explicit comparison. Sb2016 starts by defining non-isostatic topography using differences in crustal-column loads as determined from *Crust1.0* together with a mantle section integrated downward to a common depth of 100km, below the maximum thickness of any crustal column (80 km in Crust1.0) and assuming a constant sub-Moho (i.e. mantle) density $\rho_m = 3350\ kg/m^3$. *Crust1.0* includes files (.bdX, where X is a layer number) that specify the depth of interfaces of the various layers relative to the observed surface topography, thus embedding the modern topography as a reference. If isostasy pertained, all column loads (i.e. pressure) down to 100km depth would be the same. Differences in column loads reflect the non-isostatic component in the observed topography, and thus correspond with what we have referred to as 'dynamic topography=residual topography' and Sb2016 refers to as a component of the 'residual topography' (compare Sb2106 Figs. 2a, 2c, and 2d). Sb2016 actually does not explicitly derive the isostatic contribution, but instead focuses on this estimate of residual topography. We recomputed crustal non-isostatic topography (i.e. dynamic topography), starting from the observed topography, following the

Sb2016 methodology, which reproduces Fig. 2a in Sb2016. We then used the same methodology with the GIA corrected topography. A comparison of this result relative to FR2021 (in Fig. 7) is shown in Figure 8a. The differences originate in two main sources. The first is that Sb2016 applied a water loading correction, height/(ρ_m-ρ_w), for all regions in which the starting heights given by *CRUST1.0* are below 0m. The resulting differences in water load distribution, relative to our calculation in which shorelines (on the isostatic Earth) migrate to conserve water volume, are reflected in Figure 8b. The second is the difference in assumed mantle density (Figure 8c). Figure 8b shows a uniform difference in the mean depth of the oceans of -113m and mean height of regions above 0m of ~160 m, and larger differences along continental margins. In our calculations, the water load correction only applies to regions up to the height of the geoid, with a volume of water equal to the water in the oceans, hence to depths deeper than -640m. In contrast, Sb2016 applies the water loading correction to all regions that start below sea level and thus his calculation does not conserve the volume of water at the surface of the Earth resulting in local differences greater than 1900 m. The reduced water load over regions with water-loaded heights less than -640m results in relative uplift of the oceans (by 113 m) and consequent depression of the continents (by ~ 160 m) in order that the global integral equals zero is satisfied. Figure 8c shows the simple consequence of changing the assumed Moho density from the PREM value, 3380.76 kg/m^3, to 3350.00 kg/m^3 as assumed by Sb2016. The difference in assumed Moho density results in topography differences between -465 m and +141 m. It is worth noting that these two differences are generally of opposite signs over the same regions partially cancelling each other out, except along the continental margins (Fig. 8a).

Figure 8 Here

Figure 8. a) Difference between dynamic topography in figure 7, denoted "FR2021", and that derived by Steinberger (2016), denoted "Sb2016". b) Difference between FR2021 and Sb2016 dynamic topography in which the former is derived using the same sub-Moho density (3350.00 kg/m^3) as the latter. c) Difference in FR2021 dynamic topography arising from two different assumed sub-Moho densities (3380.76 kg/m^3 versus 3350.00 kg/m^3).

Others approach crustal isostasy differently. For example, Flament et al. (2013), following others, rather than computing the isostatic topography over the continents instead subtract the mean elevation of the continents (calculated by them to be 529 m) from all continental crustal areas as defined by the Müller et al. (2008) age grid and apply a depth-age correction for the oceanic crustal areas. Alternatively, Molnar et al. (2015) use a crustal density of 2670 kg/m^3 and reference column of 30 km thickness at sea level to derive their estimate of crustal isostasy. Relative to PREM, such a reference column would have an elevation of about 1530m, reflecting the significant difference in mean density of Crust1.0 crust and the reference density used in their analysis. Each of these different estimates of the crustal isostatic topography result in significant differences in estimates of the residual, i.e. dynamic, topography. Such discordances undermine the notion that the residual topography may be considered an “observable”, or a reliable datum, against which model results may be compared, unless the authors adhere to simple and straightforward definitions of this “observable”, as we advocate here.

Oceanic Crust and Lithosphere Topography – Isostatic or Dynamic?

Oceanic topography is treated quite differently by different researchers. Forte et al. (1993) treat the depth-age relationship as inherently part of Earth’s dynamic topography, as we do here. The age-dependent increase in oceanic depth is the clearest topographic manifestation of mantle convection, wherein the oceanic lithosphere represents the upper thermal boundary layer of the convective system. Flament et al. (2013) conceptually agree and state: “the bathymetry of the ocean floor is compatible with that of the thermal boundary layer of the convecting mantle, and, in this respect, the subsidence of oceanic lithosphere with age should be included in the definition of dynamic topography." However, in practice, Flament et al. (2013) exclude this component from their definition. A similar concurrence is expressed by (Steinberger 2016), but he too excludes this component from his estimate of residual topography (See his Fig. 2c). Molnar et al. (2015) also exclude ocean floor depth-age topographic variation, stating that no one questions the view that “isostatic equilibrium of the cooling lithosphere at mid-ocean ridges accounts for the variation in depth and is a process largely isolated from sublithospheric mantle dynamics…”

These differing perspectives on the dynamical treatment of shallow-mantle (sub-crustal) contributions to surface topography lead us to introduce the term “non-crustal isostasy”, which will refer to application of the isostasy principle to shallow-mantle buoyancy sources. This shallow-mantle isostasy is traditionally applied to buoyancy sources in the (oceanic and continental) lithosphere, although it has also been applied to deeper sources below the lithosphere (e.g. (Fullea, Lebedev et al. 2021)). As will be discussed in more detail below, classical isostasy applied to sub-crustal buoyancy is an approximation whose accuracy diminishes substantially with increasing thickness of the shallow-mantle layer (see also Appendix B).

We emphasize here that a fundamental conceptual conflict arises when depth-age is excluded from the dynamic topography, as was originally pointed out by (Forte, Peltier et al. 1993). The predicate of isostasy is that the mantle is hydrostatic and therefore not convecting, and yet the mid-oceanic ridge itself, and the thermal anomaly that is being advected with the plates that gives rise to the depth-age relationship inherently requires convection. This applies as well to (Wang, Liu et al. 2022) who use mid-oceanic ridges as the global isostatic reference, stating that a ridge “consists of a simple mass column (oceanic crust overlying the ambient mantle) and is at a hydrostatic state relative to the low-viscosity mantle underneath." Adopting this reference frame ignores that ridges are inherently dynamic structures that only exist because the mantle is convection, in contradiction to the predicate of isostasy itself. This reference choice also inverts the sign of the effect of cooling with age. Ridges stand ~3550 m above old ocean floor (~175 Ma based on Rowley, 2018). In this framework mid-oceanic ridges have negative and old oceanic lithosphere has positive residual topography (Wang et al. 2022, their Fig. 2A). In the general framing (Forte et al. 1993, Steinberger, 2016, and above), ridges represent a positive contribution to non-crustal isostatic topography such that subsidence with age brings the oceanic crust closer to crustal isostatic equilibrium as shown in Fig. 3. From the global integral equals zero perspective, the Wang et al. (2022) recommended change in reference has a profound impact as the continents are relatively elevated by >1000m and oceanic lithosphere depressed by ~-633m, and with ridges (age≤5.0Ma) in particular depressed by ~-1930m relative to Fig. 7.

The dynamical importance in terms of ridge-push of the evolving thermal structure of the oceanic lithospheric with age was also highlighted long ago by Richter (1973) and (Hager and O'Connell 1981) in their studies of plate-driving forces. Thus, decoupling this dynamical lithospheric component and effectively treating it as existing in the absence of mantle convection is physically incoherent.

Despite the above considerations, the depth-age component of the oceanic topography is often excluded from dynamic topography analyses and is included as a separate mantle lithosphere "isostatic" contribution to the topography. However, even when adopting this perspective, there is a question as to which depth-age model to employ for the oceanic lithosphere and how to dovetail age depth corrections with adjacent continental crust, specifically along passive continental margins. Should a square-root age model reflecting half-space cooling be removed (Spasojevic and Gurnis, 2012, Steinberger, 2016), or some "plate" model characterized by decreasing subsidence with age be subtracted?

Figure 9 Here

Figure 9. Depth-age models of the oceanic lithosphere modified from (Rowley 2018). Thick solid red is best-fit plate model to the median of the depth-age data associated with actual age picks derived from marine magnetic anomalies (Rowley, 2018), with associated fits to ±1σ distributions in thinner red. Darker blue is best fit half-space cooling constrained by picks younger than 84Ma and lighter blue half-space cooling at all ages. Orange is plate model of Hoggard et al. (2016). Dashes are from (Stein and Stein 1992), and dots are (Crosby and McKenzie 2009).

Rowley (2018) used the 'Global Seafloor Fabric and Magnetic Lineation' (GSFML) data set (Seton, Whittaker et al. 2014) that includes locations of approximately 100,000 magnetic anomaly picks, to derive fits (shown in Figure 9) to a range of metrics, including median, mode, mean, and ±1σ and ±2σ sediment-load corrected depth deviations at each magnetic anomaly pick age for the main ocean basins (excluding back-arc basins). These picks represent the vast majority (~99%) of locations on the ocean floor that have explicitly constrained oceanic crustal ages, and thus provide the only global dataset from which to derive a robust depth-age relationship from data, not model ages. Rowley (2018) also derived a new sediment load-correction of oceanic sediments based on more than 9 million wet-bulk density measurements from deep sea drilling cores. From these data it is clear that the best fit sediment-load corrected model is a plate model.

Spasojevic and Gurnis (2012) removed a half-space cooling model, fit to oceanic lithosphere ages less than or equal to 70 Ma published by (Parsons and Sclater 1977), but applied to all ages. That half-space depth-age relationship is similar to that shown in Fig. 9, which is a fit to ages ≤ 84 Ma (Rowley, 2018). Steinberger (2016) subtracts a square root age model based on (Korenaga and Korenaga 2008), who derived their estimate using ages based on the 1997 version of the age grid (Müller, Roest et al. 1997), for ages less than 100 Ma, and a constant offset of -3300 m from the ridge depth for older ages as discussed further below. Alternatively, one could use a best fit half-space cooling model for all ages (Fig. 9), but this has not been used in any analyses that we are aware of. Flament et al. (2013) subtract a lithosphere cooling model by Crosby and McKenzie (2009) (Figure 9), characterized by a rise and fall in the predicted ocean depth in the Cretaceous, which Rowley (2018) shows is unsupported by GSFML and sediment load-corrected ocean drilling data, or a more recent age grid model (Müller, Seton et al. 2016). Hoggard et al. (2016) remove a plate model that they derived (Figure 9). The differences among these models are as large as several hundred meters: a magnitude that corresponds with some estimates of the maximum amplitude of dynamic topography (e.g. Hoggard et al. 2016, Molnar et al. 2015). It is thus evident that subtracting these different models will not only impact the magnitude of estimated dynamic topography, but also its sign, thereby exacerbating the uncertainty generated by effectively arbitrary choices made by different research groups to differentiate isostatic versus non-isostatic or dynamic topography. We finally note that these previous studies use age-grid models, but these too have issues when compared with the direct magnetic anomaly pick data, as demonstrated by Rowley (2018).

Another problem with the approaches discussed above is that oceanic lithosphere has considerable variation in depths at all ages. According to Rowley (2018): 1) zero-age lithosphere has an 8 km range of elevations; 2) there is some correlation of deeper ridge flanks with deeper ridges, hence depth at age has some correlation with starting depth; 3) there is some correlation of ridge depth with full spreading rates less than about 70 mm/y; and 4) there is some correlation between ridge depth and crustal thickness making it unclear what constitutes anomalous bathymetry, or whether removing the best fit mode, mean, or median, with or without including ±1 sigma distributions or half-space cooling is most appropriate, were one to employ such an approach.

Figure 7 emphasizes that dynamic/residual topography across passive-type continent-ocean boundaries (COB) is continuous and regardless of the age of the adjacent oceanic lithosphere. Removing oceanic depth-age topography introduces an arbitrary step function boundary along COBs. It is easiest to highlight this effect using Steinberger (2016) as he is explicit about the various components incorporated in his definition of residual topography. As mentioned above, Steinberger (2016) provides the following relationships:

$$h_{th} = h_0 - 330\sqrt{age(Ma)}\text{, for oceanic ages} < 100\ Ma$$

$$h_{th} = h_0 - 3300\text{, for oceanic ages} > 100$$

$$h_{th} = h_0 - 4365\text{, for undefined age,}$$

where h_{th} is the height of each grid cell, and h_0 is chosen such that the integral of h_{th} has zero global mean. The third equation applies to all regions with no assigned ages, hence includes continental crust. What is immediately obvious is that COBs will demarcate locations with an abrupt deepening of ≥1065 m in the modeled residual topography, and for very young COBs an offset of ~4365m (see Fig. 10b). The magnitude of this step change in modeled residual topography will vary based on the particular depth-age model adopted but since data from the continents are excluded, all non-ocean grid cells are compelled to have a single value that must offset the positive residual topography of MORs to satisfy the global integral constraint. Furthermore, although this correction itself has a zero global mean, the heights of all continental regions are uniformly depressed in order to match this constraint, whereas in the real world the crust and mantle lithosphere vary spatially to yield a continuous gradient in isostatic and dynamic/residual topography across these COBs.

The preceding discussion again highlights the rationale for modelling all mantle lithosphere globally, incorporating both thermal and chemical contributions to density and hence as part of joint seismic and geophysical inversions for present day dynamic topography (Forte et al., 2015; Lu et al., 2020). As discussed above, we treat all topography not accounted for by crustal isostasy as dynamic topography, and thus seek to account for all residual topography in the oceans as related to the direct consequences of mantle convection, affecting both the lithosphere and underlying mantle.

The discussion above has revealed differences in previously adopted definitions of the isostatic topography, resulting in substantial differences in the topography component that needs explanation from non-crustal isostatic sources. What is often difficult to recognize is the magnitude of the differences that are embedded in various estimates of these other non-crustal isostatic sources of topography. Below we explore these to highlight the components of Earth's topography that are often hidden within or inherent in these other treatments.

Residual Topography

Similar to isostatic topography, the term residual topography has also varied considerably in meaning, depending upon the author. We equate this term, following Forte et al. (1993), to dynamic topography, which is simply the difference between the observed or GIA-corrected topography and crustal isostatic topography that is mapped, for example, in Figure 7. This straightforward definition provides an explicit context for quantifying the sources and contributions to Earth's topography.

In other assessments of the contributions to Earth's topography, the term residual topography, when assessed separately from dynamic topography, is usually regarded as an "observed" component of the topography. Figure 10 shows residual topography fields, one of which is obtained by subtracting Rowley (2018) age-dependent ocean bathymetry from FR2021 (Fig.7), along with several published estimates of residual topography (Steinberger 2007, Flament, Gurnis et al. 2013, Steinberger 2016, Hoggard, Winterbourne et al. 2017, Steinberger, Conrad et al. 2019) that provide a basis for interpreting components included in the "explained" aspects of Earth's topography versus what remains to be explained by dynamic topography. Note that Steinberger (2016) (Fig. 10c) interpolates values in regions of LIPs, whereas Fig. 10a does not. To asses these aspects, we use the published grids (Flament et al. 2013, Hoggard et al., 2016, (Steinberger, Conrad et al. 2019) regridded to pixel-centered one-arcdegree grids identical with Crust1.0 and corresponding GIA-corrected topography (Figure 2).

Figure 10 Here

Figure 10. Five residual topography estimates for the present-day Earth. Color scales are the same for each map. Residual topographies from: a) FR2021 (fig. 7) from which age-dependent oceanic topography derived by Rowley (2018) (fig. 10b) has been removed, b) Rowley (2018) depth-age paired with continent value derived from Steinberger (2016), c) Steinberger (2016) represented by fig. 2c in that paper, d) Flament et al. (2013), e) Hoggard et al. (2016), and f) Steinberger et al. (2019) that shows the air-loaded residual topography. The age-dependent lithosphere topography reduction in (a, b) and (c) assume a continental elevation of -1187m, based on Steinberger (2016) age-dependent and undefined (~continental crust) equations. g) Root-mean-square (rms) amplitude of dynamic and lithospheric topography, as a function of spherical harmonic degree, from FR2021 (fig. 7) and Rowley

(2018) and from Steinberger (2016) (figs. 2b and 2c in that paper). h) Rms amplitude of residual dynamic topography, as a function of spherical harmonic degree, for fields shown in maps (a), and (c) to (e).

The residual topographies, for example, in Fig. 10 are usually treated as "observables" that can be compared with an independently calculated dynamic topography. Flament et al. (2013) compute the residual topography by removing the mean continental elevation (529 m) from continental crust, which includes all elevations above approximately -200m corresponding to the continental shelves. Over the oceans they subtracted the Crosby and McKenzie (2009) depth-age curve from sediment load corrected bathymetry. Hoggard et al. (2016) derived their residual topography over the oceans using deviations from their depth-age model where they find a correlation with long wavelength (>700 km) free-air gravity anomalies using an admittance of Z=25±10 mGal/km, to which they add primarily admittance-derived estimates of residual topography over the continents, assuming a constant air-loaded admittance of Z=50 mGal/km. They make some additional adjustments using drainage patterns and remove continental estimates within 500 km of oceanic residual depth determinations. Steinberger (2016) combines Crust1.0 non-crustal isostatic topography (see above-his Fig. 2a) with depth-age equations given above to derive this estimate of residual topography (his Figs. 2c,d). We note, in this context, that Steinberger (2016) also presents (his Fig. 6d) an alternative representation of long-wavelength residual topography in which the ocean age correction is not applied, but analyses of fits between predicted (model) topography and residual topography include the age correction. Finally, Steinberger et al. (2019) combine Steinberger (2016) over the continental crust with Hoggard et al. (2016) over the oceans.

Given the differences in approaches, it is not surprising that these residual topography maps are different. Indeed, one of the primary objectives of determining the residual topography is to set a basis for evaluating the fit of dynamic topography derived from mantle flow, where the latter is modelled to fit the former. Consequently, the differing definitions of residual topography helps to explain the contrasts between different model calculations of dynamic topography. As discussed above, an important source for these differences is the model adopted to represent the age-dependent bathymetry of the oceans and the assumed equilibrium elevation of continents. This "lithospheric" signal is large and is comparable to that of dynamic (non-isostatic crustal) topography, as is clearly evident in the wavelength-dependent spectral amplitudes of both fields shown in Fig. 10g. Here we compare the spectral amplitudes of both FR2021 and Sb2016 dynamic topography fields with the corresponding spectral amplitudes of age-dependent lithospheric topography as determined by Sb2016 (his Fig. 2b) and by Rowley (2018), where in the latter case we adopt the same value of lithospheric topography of continents as in Sb2016. The similarity of the amplitudes of dynamic and "lithospheric topography" highlights the potentially large uncertainties that can arise when these two fields are subtracted to infer the smaller-amplitude residual topography fields, shown in Fig. 10h. The relative differences between these estimates of residual topography are larger than the relative differences between dynamic topography estimates (Fig. 10g).

To aid in a quantitative comparison of the maps in Fig. 10, we plot in Fig. 11 the spatial correlations of these residual topography maps, starting with the correlation between the FR2021 dynamic topography (Fig. 7) and the Sb2016 dynamic topography (his Fig. 2a). For consistency we plot correlations (Fig. 11) of residual topography estimates that have been smoothed by truncating their spherical harmonic expansion at degree ℓ =30. Figure 11a shows that there is a close correlation of what Steinberger (2016) describes as non-isostatic topography derived from *Crust1.0* and what we call dynamic topography also derived from *Crust1.0*. The deviations from 1:1 correlation reflect regions on continental margins where water load corrections applied by Steinberger (2016) do not account for shoreline migration relative to background isostatic topography (Fig. 3). Figure 11b compares the residual (FR2021-this study dynamic-R2018 lithospheric) topography of FR2021 (Fig. 10a) against Sb2016 (Fig. 10c), and we note that the correlation is now reduced relative to that in Fig. 11a, which highlights the increased uncertainties inherent in estimating residual topography when sources beyond crustal isostasy are included. Sb2019 is constructed by combining the residual topography from the continents and deviations from the depth-age model from Hoggard et al. (2016) for the oceans, and hence is similar in construction to FR2021-R2018. Although the correlation between residual Sb2016 and FR2021, Sb2016 Fig. 2c vs. FR2021-R2018, and Sb2019 vs. FR2021-R2018 (Fig. 11a-c) are good (>0.84), the other correlations (Figs. 12d-f) are poor, with values between 0.191 and -0.048. An alternative quantification of agreement is provided by the relative misfit, which is equal to the rms difference between the predicted topography fields normalized by the rms amplitude of predicted topography. This measure of misfit depends on both the spatial correlation and the amplitude of topography. The relative misfit between smoothed FR2021 and Sb2016 residual topography (Fig. 11b) is 30%, whereas for the other comparisons (Figs. 11d-f) it exceeds 100%. Given such low levels of agreement, it is not surprising that associated models of dynamic topography interpreted in terms of mantle flow calculations, are themselves quite different.

Figure 11 Here

Figure 11. Correlations of residual topography topography estimates with a bin size of 250 m. All plots are filtered at maximum spherical harmonic degree 30: a) Steinberger (2016, his fig. 2a) with FR2021 (fig. 7). b) residual topography of Steinberger (2016, his fig. 2c) versus residual FR2021-R2018 topography (fig. 10a), c) residual topography of Steinberger et al. (2019) , d) Flament et al. (2013), and e) Hoggard et al. (2016) versus residual FR2021-R2018, f) Hoggard et al. (2016) versus Flament et al. (2013).

One of the fundamental problems is that mantle lithosphere density and thickness are significantly more poorly constrained than crustal properties, particularly under the continents where direct evidence from studies of mantle xenoliths provides limited spatial sampling (Kaban, Schwintzer et al. 2003). Moreover, assessments of large-scale buoyancy range from at least locally positive (Kaban, Schwintzer et al. 2003), to neutral (Jordan 1975, Jordan 1988) to negative (Forte and Perry 2000, Kaban, Schwintzer et al. 2003). In contrast, modelling the density of the oceanic lithosphere mantle is, at least in theory, straightforward.

As discussed above, we include all mantle lithosphere contribution to Earth's topography in our definition of dynamic (= residual) topography. This definition requires that any acceptable model of sub-crustal density anomalies, at all depths in the mantle, must be in accord with global seismic tomography and simultaneously fit an array of geophysical global observables that include free-air gravity anomalies, excess ellipticity of the core-mantle boundary, present-day plate motions, and dynamic topography each with their own sensitivities as explained by Forte et al. (2015) and employed by Simmons et al. (2009, 2010) and Lu et al. (2020). These solutions are typically characterized by negative buoyancy of most continental roots that are included in the definition of dynamic topography we adopt.

While Flament et al. (2013), following (Gurnis 1993), recognize that oceanic depth-age should be included in the definition of dynamic topography, they nonetheless state: "the dynamics of the continental lithosphere are more complex and cannot be explained by boundary layer theory. For this reason, defining dynamic topography globally as the difference between observed topography and isostatic crustal topography (e.g., (Forte, Peltier et al. 1993, Forte, Peltier et al. 1993) results in continents dynamically depressed by up to 3 km, which is inconsistent with observations" citing Gurnis (1993). Gurnis (1993) predicated this argument on the observation that the long geological record of continental inundation by sea water is inconsistent with large amplitude depressions exceeding ~300 meters. However, the cratonic mantle lithospheric roots are dynamic in the sense that they are horizontally advected with the plates, as is true of the oceanic lithosphere mantle, and that changes in thickness or density of these mantle lithospheric roots gives rise to changes in surface topography independent of changes in crustal thickness or crustal density. Thus, advection of the mantle lithosphere with the plates maintains the depression of the continents on timescales of the ages of these roots and in proportion to their density contrast with the mantle at equivalent depths, again identical with the oceanic lithosphere. This negates the argument put forth by Gurnis (1993) and reiterated by Flament et al. (2013), among others. As discussed in Forte et al. (1993, their Reply), the amplitude of changes in dynamic topography differs from the amplitude of instantaneous (e.g. present-day) dynamic topography, such that geologic (inundation) data constrain the former, not the latter. This point has also been discussed by Steinberger (2016). The continents remain at or near sea level because they are maintained there by the long-term preservation of the continental mantle lithosphere roots. When those roots are dynamically removed, through some sort of gravitational instability, the surface topography increases, as for example under the Colorado Plateau and Great Basin region, eastern North China, and parts of the eastern seaboard of the US, among other regions. It is worth noting that the gravitational instabilities such as drips or delaminations are activated because the mantle lithosphere is more dense than the underlying mantle. In summary, there is no contradiction between continental flooding records and large-scale continental depressions that we define as a component of instantaneous (present-day) dynamic topography.

Limitations of Admittance Analysis

Finally, we consider Molnar et al.'s (Molnar, England et al. 2015) criticism of current estimates of dynamic topography. Molnar et al. (2015) argue that because observed free-air gravity anomalies are small, and isostatic anomalies are even smaller, that mantle flow induced normal stresses acting at the base of the lithosphere do not result in greater than ~300m of deflection, thereby limiting dynamic topography to within this amplitude. It is important to recognize the key role that Molnar et al. (2015) place on free-air gravity anomalies as the arbiter of their estimates of the amplitude and location of any and all dynamic topography. They state: "Much more important for geodynamics than labels is an understanding of the degree to which normal tractions applied to the base of the lithosphere by convection support the topography. Because the building of tectonic features requires that work be done by or against gravity, we, as do many … (long list of citations), consider gravity anomalies to offer the tightest constraints on the degree to which surface topography results from normal tractions applied to the base of the lithosphere" (p.1934). Molnar et al. (2015) then predicate their analysis of the amplitude of topography associated with mantle flow induced normal stresses acting at the base of the lithosphere based on observed free-air gravity anomalies. They derive a rule of thumb admittance, common to many other such analyses (e.g. Hoggard et al. 2016), of about 50 mGal/km.

The problem with this translation of gravity anomalies by a rule of thumb admittance, is that for a complex mantle viscosity structure, this rule of thumb is inappropriate. (Forte 2007, Forte, Simmons et al. 2015) describe the fundamental connections between surface geophysical observables and mantle flow, and how they are applied in constructing seismic tomographic models that simultaneously solve for 3D seismic velocity and density structure of the silicate Earth. The geophysical observables sensitive to mantle buoyancy variations include free-air gravity, dynamic topography at Earth's surface and at the CMB, as well as plate motions. It is worth recalling that the succession of geodynamically constrained seismic tomography and density models published by (Simmons, Forte et al. 2006, Simmons, Forte et al.

2009, Simmons, Forte et al. 2010), and most recently (Lu, Forte et al. 2020), are based on the mantle-dynamic framework presented in (Forte 2007, Forte, Simmons et al. 2015). This framework ensures that all of their tomography-based mantle flow models simultaneously satisfy the free-air gravity data and estimates of dynamic topography derived from differencing the observed and crustal isostatic topography, thus making the arguments put forth by Molnar et al. (2015) entirely moot.

The reader is directed to (Forte 2007, Forte, Simmons et al. 2015) for more details concerning the relationship between geodynamic observables (e.g. topography and gravity) and mantle flow induced by density perturbations in a mantle with a complex depth-dependent viscosity. In these flow calculations, the kernel functions that describe the wavelength-dependent connection between internal density anomalies and surface observables are explicitly provided. One of the important characteristics of the free-air gravity kernels is their complex depth-dependence that involves changes in sign due to changes of viscosity with depth. This precludes the use of the simple admittance estimates employed in Molnar et al. (2015), which itself is based on classical analyses by (McKenzie 1977) and earlier, in which the mantle is treated as an isoviscous fluid. This point has also been made more recently by Yang & Gurnis (2016) and by Coli et al. (Colli, Ghelichkhan et al. 2016) using viscous flow models of the mantle.

This point is further illustrated by Fig. 12a that shows the spatial correlation of observed free-air gravity (Tapley, Ries et al. 2007) and Crust1.0 based modeled dynamic surface topography from Lu et al. (2020), where both are represented up to spherical harmonic degree 32, corresponding to the long-wavelength spatial scales analyzed by Molnar et al. (2015). We employ the computed dynamic topography in order to demonstrate that computed mantle flow is capable of generating the observed dynamic topography and be consistent with free-air gravity constraints. The corresponding estimates of admittance based on these data are presented in Fig. 12b. It is clear from Fig. 12a that km-scale dynamic topography can correspond to zero free-air gravity anomalies and that there is no correlation (R=-0.005) of admittance and amplitude of dynamic topography (Fig. 12b) as assumed in Molnar et al. (2015), among others. In summary, the admittance rule of thumb employed by Molnar et al. (2015), Hoggard et al. (2016) and others, cannot be applied because the mantle is not isoviscous.

Figure 12 Here

Figure 12. a) Free-air gravity anomaly (Tapley et al., 2007) versus Crust1.0 derived dynamic topography both represented to degree 32 (Lu et al. 2020) and sampled on the Crust1.0 grid with a bin size of 250 m for dynamic topography and 10 mGal/km for gravity. B) Estimates of admittance based on 12a.

Dynamic Topography Models

All agree that dynamic surface topography is the result of normal stresses acting on the solid-surface, thus displacing this surface away from the position predicted by isostasy. An important and often little emphasized aspect of differences in past models of dynamic topography is the specification of exactly at what depth or material boundary, above which the isostatic support of subsurface density anomalies is assumed. According to our definition, that boundary is the Moho, thereby limiting the isostatic contributions to surface topography to crustal heterogeneity only. As highlighted above, this puts all subcrustal contrasts in density and thickness of the lithospheric mantle within the dynamic topography component of the topography. In past studies, there is an additional sub-crustal layer in which density anomalies are also assumed to be in isostatic equilibrium. The (sometimes arbitrary) depths to which isostasy is assumed include: the base of the lithosphere at ~100 km (Molnar et al. 2015), 220 km (Steinberger 2007, Müller, Sdrolias et al. 2008), 250 km (Spasojevic and Gurnis 2012), 300 km (Conrad and Husson 2009), 350 km (Flament, Gurnis et al. 2013, Young, Flament et al. 2022), or 400 km (Afonso, Salajegheh et al. 2019, Fullea, Lebedev et al. 2021). In most of these studies that employed seismic tomography models to represent mantle heterogeneity, the adoption of separate age-dependent, and in some cases isopycnic (e.g. under continents), representations for sub-crustal contributions to isostatic topography involved "zeroing out" all density anomalies above the lower boundary chosen for the isostatic layer. The choice of this boundary has important consequences: (1) There is a direct relation between thickness of the layer and the minimum wavelength of the resulting dynamic topography; and (2) removing mantle heterogeneity between the Moho and approximately 200 to 350 km removes about 50% of the total dynamic topography (Forte et al. 2015) that manifests surface boundary layer dynamics. It is also important to note that once this boundary is specified, all regions shallower than the boundary are effectively treated as belonging to an isostatic layer that may be substantially thicker than thermally defined lithosphere (especially for boundary depths > 100 km). In Appendix B we present a detailed evaluation of the dynamic implications of assuming isostatic support for density heterogeneities in a shallow-mantle layer of variable thickness.

The deeper (> 100 km) isostasy models remove dynamical contributions from some or all of the asthenospheric low velocity zone, a region with the lowest or among the lowest mean viscosities of the mantle (Mitrovica and Forte 2004), and hence characterized by high deformation rates, which violates the isostasy assumption. Although the Forte et al. (2015) estimate of shallower mantle contributions to dynamic topography includes depth-age variations, there are non-trivial shallow, asthenospheric sources of buoyancy unrelated to depth-age that are neglected when these deeper boundary layers are chosen. Examples include the source of the Pliocene Orangeburg Scarp shoreline deflection along the east coast of the US (Rowley, Forte et al. 2013), and western south Pacific across the *SOPITA* volcanic province (Rowley, Forte et al. 2016) and western equatorial Pacific (Campbell, Moucha et al. 2018). Finally, not surprisingly, models that employ deeper compensation depths are characterized by much longer wavelength, effectively hemispheric scale estimates of dynamic topography uncorrelated with surface plate tectonics, but instead correlated with topography (and geoid) highs over the Pacific and Atlantic plus Africa, and lows associated with circum-Pacific subduction under South America/northern North America and western Pacific/southeast Asian regions (Figure 13).

Figure 13 Here

Figure 13. Models of dynamic topography. a) This study based on viscosity profile V1 and new inversion of Lu et al. (2020) up to l=128, b) Steinberger (2007), c) Conrad and Husson (2009), d) Spasojevic and Gurnis (2012), e) Flament et al. (2013), and f) Steinberger (2016-Fig. 6c) up to l=128 and rescaled by 1.45 over the oceans to respresent water-loaded dynamic topography as in Lu et al. (2020). Color scale is the same for all images.

The maps in Figure 13a through f are computed present day dynamic topographies, but it is important to recognize that each is derived in a different way and with different assumptions as to the depth of the boundary above which the material is treated as effectively isostatic, as noted above. Figure 13a is based on Lu et al. (2020) that follows Forte et al. (2015) description of a full joint seismic-geodynamic tomography inversion that significantly updates previous versions (Simmons, Forte et al. 2006, Simmons, Forte et al. 2009, Simmons, Forte et al. 2010). The latest joint tomography models by Lu et al. (2020) provide optimal fits to dynamic topography (Fig. 7) and free-air gravity data up to degree 32, incorporating mineral physics and geodynamic constraints on the 3-D density-velocity scaling, for a range of viscosity models. Note that the scaling of shear wave velocity to density includes both thermal and non-thermal (i.e. compositional) contributions and therefore varies in 3-D throughout the mantle to yield the best fit to the geodynamic observables that include dynamic topography (Fig. 7). This explicit joint inversion approach strongly departs from others and explains why the resulting modeled dynamic topography (among other components, such as mantle flow) differs, often markedly, with other predictions. One contributor to these differences relate to the scaling of seismic velocity anomalies to density. For example, Steinberger (2007) uses a purely depth dependent velocity-density scaling that remains close to 0.25 g cm^{-3} km^{-1} s throughout the mantle and thus effectively treats all density anomalies as thermal in origin. Similarly, Conrad and Husson (2009) scale the S20RTS (Ritsema, van Heijst et al. 2004) shear wave velocity anomalies to density anomalies with a constant value (0.15 g $cm^{-3}km^{-1}s$). Spasojevic and Gurnis (2012) cite (Spasojevic, Gurnis et al. 2010) to also scale S20RTS (Ritsema, van Heijst et al. 2004) shear wave velocity anomalies, but are not explicit about which of the various scalings discussed they actually used in their model, although

Flament et al. (2013) state that it varies radially from 0.05 to 0.3 g cm^{-3} km^{-1} s and they too effectively treat all density variations as thermal in origin.

Flament et al. (2013) and (Young, Flament et al. 2022) do not employ a tomography model, but rather used a mantle flow model driven by imposed surface velocities that integrates both present and past plate motions, the details of which are described in their paper, thereby producing a dominant contribution from subducted slab heterogeneity in their prediction of the present-day dynamic topography. This modelling approach implies that the dynamics of mantle convection, that is the forces driving both the plates and the large-scale flow in the mantle, is largely if not entirely related to plate convergence, thereby minimizing mantle flow contributions driven by active buoyant upwelllings, see Rowley et al. (2016) and (Rowley and Forte 2022) for arguments supporting significant contributions from these active buoyant upwelling to plate driving forces.

Steinberger (2016) provides a range of different modeled dynamic topography of which Fig. 13f derives from his Fig. 6c that includes modeling seafloor topography with water loading and thus most closely matches Lu et al. (2020).

Because all of the models start with an "observed" residual topography model, it is not surprising that the predicted dynamic topography is correlated with those estimates. In order to help visualize the differences we again use correlation plots of modeled dynamic topography (Fig. 14). Figures 14a through 14e are correlations relative to the model of Lu et al. (2020), whereas 14f compares Flament et al. (2013) to Spasojevic and Gurnis (2012) to demonstrate that the limited correlations are not due to choice of the reference model. We again limit the correlations to spherical harmonic wavelengths $\ell \leq 30$ reflective of the generally smooth, long-wavelength characteristic of most models of dynamic topography. Figure 14 makes it clear that there is generally little correlation among these models and therefore little or no consensus as to the underlying mantle flow dynamics. The closest comparison is between Steinberger (2016) with Lu et al. (2020) (Fig. 6e).

Figure 14 Here

Figure 14. Correlations of dynamic topography from mantle flow calculations (a-e) relative to Lu et al. (2020). a) Steinberger (2007); b) Conrad and Husson (2009) c) Spasojevic and Gurnis (2012); d) Flament et al. (2013); e) Steinberger (2016, Fig. 6e); and f) Flament et al. (2013) relative to Spasojevic and Gurnis (2012). Correlation coefficients (R) are provided in the lower right corners. Colors represent percent with a bin size of 250m in both directions relative to 64800 total grid cells. All models are represented up to spherical harmonic wavelengths of $l \leq 30$.

Limitations of Isostasy

Past modelling of Earth's topography in terms of isostatic contributions from density anomalies in the shallow mantle, extensively reviewed above, suggests that shallow sources are dominant and that density anomalies in the deeper mantle, with the important exception of the longest wavelengths (e.g. Forte 2007, (Yang and Gurnis 2016), have much smaller or negligible contributions. The past models have employed differing estimates for the thickness of the isostatic layer below the crust, where the most recent studies assume the bottom of this layer may be as deep as 400 km (Afonso, Salajegheh et al. 2019, Fullea, Lebedev et al. 2021). Here we examine more closely the dynamical justification for employing thick layers (> 100 km) for modelling isostatic topography, which will lead to a reevaluation of the relative importance of shallow- verses deep-mantle contributions to dynamic topography (discussed in the next section).

In this analysis, we employ a viscous flow model of the mantle that incorporates 3-D thermochemical density anomalies derived from joint inversions of global seismic and geodynamic data, which include mineral physics constraints (Lu et al. 2020). This flow model, which was employed in the dynamic topography prediction presented above in Figure 13a, also incorporates the coupling of mantle flow to rigid tectonic plates whose rotations are determined by the underlying mantle flow, not vice-versa (Forte 2007). In the following, it is also worth noting that the mechanical feedback of strong plates provides an important dynamical stabilization of shallow density anomalies. This stabilization extends the validity of the isostatic equilibrium approximation to greater depth than with the standard, free-slip (i.e. fully yielding) surface boundary condition (see Appendix B). As noted above, in the discussion of equation (22), the isostasy assumption requires that lateral pressure perturbations, relative to the global (horizontally averaged) mean pressure, must everywhere equal zero at the base of the layer.

We now consider a mantle layer, immediately below the crust, which may have three possible thicknesses: 100 km, 200 km, and 400 km. The density anomalies in this shallow layer will be taken from the Lu et al. (2020) global tomography model and we assume zero density anomalies in the mantle below the layer. For the depth-dependent viscosity structure of the mantle, we employ the viscosity profile derived by Mitrovica and Forte (2004) from a joint inversion of mantle convection and GIA data. We next calculated the equilibrium response of the mantle to the buoyancy distribution in the shallow layer, employing the theory of a compressible, self-gravitating, viscous fluid in a spherical shell (Forte 2007). For each of the three thicknesses cited above, we calculated the solid-surface topography that is in dynamical balance with the integrated loads in the shallow mantle layer. If isostasy obtains, the topographic loading plus the vertically integrated loads within the layer should yield no lateral pressure variations at the bottom of the layer (as required by eq. 22).

In Table 1, we summarize our testing of this isostatic approximation by tabulating the dynamic pressure variations below the shallow layer and compare their magnitudes with pressure variations acting directly below the solid surface (i.e. at the top of the shallow mantle layer), where the latter induce the topographic deflection of the surface. A dynamic pressure perturbation of 10 MPa will induce a 460-m vertical displacement of the solid surface (assuming an overlying water layer). The dynamic pressure in the shallow layer and underlying mantle are determined by calculating the viscous response to the density loads within the shallow layer. We find the global root-mean-square (rms) amplitude of dynamic pressure variation predicted at the base of a 100-km thick layer is only 4% of the surface value, indicating isostasy is a reasonably accurate assumption for this thickness. (Perfect isostasy of course requires 0%.) For a 200-km thick layer, the rms basal dynamic pressure variation is almost 8% of the surface value, while for a 400-km thick layer it is 18%. We thus observe a notable reduction in accuracy of the isostasy approximation when layer thickness increases beyond 100 km.

Table 1: Dynamic Pressure Variations in a Shallow-Mantle Layer

Layer Thickness = 100 km						**Layer Thickness = 200 km**						**Layer Thickness = 400 km**					
depth = 3 km			depth = 110 km			depth = 3 km			depth = 210 km			depth = 3 km			depth = 425 km		
max	*min*	*rms*	*max*	*min*	*rms*	*max*	*min*	*rms*	*max*	*min*	*rms*	*max*	*min*	*rms*	*max*	*min*	*rms*
21	-18	5	0.8	-0.8	0.2	35	-41	12	3	-3	0.9	64	-62	19	14	-12	3.5

Note: "max, min, rms" denote maximum, minimum and root-mean-square, respectively. Values are in MPa.

In the context of isostasy, the requirement for no pressure perturbations in the underlying mantle naturally implies that no viscous flow should be excited in the mantle, since the latter is inconsistent with hydrostatic equilibrium in the underlying mantle. In figure 15 we present maps of the mantle flow excited by departures from perfect isostasy in the shallow mantle layer. When the layer thickness is 200 km (Fig. 15a) we find the rms amplitude of horizontal flow at 210 km depth is 0.6 cm/yr, which is 14% of the rms amplitude of present-day tectonic plate motions in the no-net-rotation reference frame, which is 4.3 cm/yr. For 400 km layer thickness, the rms amplitude of horizontal flow produced at 425 km depth (Fig. 15b) is 20% of the present-day plate motions. We note these relative amplitudes are similar to those obtained from Table 1, in accord with the expected dynamical correspondence between horizontal flow amplitude and pressure perturbations below the shallow-mantle layer.

Figure 15 Here

Fig. 15. Viscous flow excited by shallow-mantle layers. In a) and b) the thickness of the layers is 200 and 400 km, respectively. The density anomalies inside the layers are given by the global tomography model of Lu et al. (2020) derived by jointly inverting global seismic, geodynamic and mineral physics data. In each case, density anomalies are removed from the entire mantle below the layer. The predicted mantle flow in a) and b) is calculated at a depth of 210 and 425 km, respectively, employing the radial viscosity profile derived by Mitrovica and Forte (2004). The mechanical feedback of rigid, freely rotating tectonic plates is included in the flow calculations (Forte 2007). The root-mean-square (rms) amplitude of horizontal flow is indicated below each map. All fields are represented by a spherical harmonic expansion truncated at degree $\ell = 32$.

Shallow- Versus Deep-Mantle Contributions to Dynamic Topography and Gravity Anomalies

It is evident from Table 1 and Fig. 15 that deviations from isostasy become increasingly important as the thickness of the shallow-mantle layer increases, especially for a thickness of 400 km that has been employed in recent modelling of upper-mantle heterogeneity (Afonso, Salajegheh et al. 2019, Fullea, Lebedev et al. 2021). These recent studies assume this upper-mantle layer is in isostatic equilibrium and also that it is sufficient to only consider density anomalies within the layer, including the overlying crust, to fully model Earth's global topography and anomalous gravity fields, where the latter are high-pass filtered to approximately remove contributions from density anomalies below this layer. This modelling of surface topography and gravity variations in terms of density anomalies contained in a shallow upper-mantle layer requires that deeper-mantle contributions to these fields be negligible. To directly evaluate the justification for this assumption, we again turn to the tomography-based mantle flow model employed above in Figs. 13a and 15. The solid-surface undulations (i.e. dynamic topography) driven by density loads contained everywhere below 400 km depth (Fig. 16b) have an rms amplitude that is more than 50% of the topography amplitude induced by loads in a shallow 400-km thick layer (Fig. 16a). Moreover, we find that assuming pure isostasy overpredicts the amplitude of topography induced by loads in the shallow layer by 19% (Fig. 16f), relative to a dynamically consistent prediction (Fig. 16a). The isostatic prediction of topography, employing density anomalies in the top 400 km of the mantle, provides a 69% variance reduction to the FR2021 crust-corrected topography (Fig. 7). This compares with a 77% variance reduction obtained with a fully dynamic calculation of topography driven by density anomalies at all depths (sum of Fig. 16a & 16b), and a 66% variance reduction when the dynamic topography is driven only by density anomalies in the top 400 km of the mantle (Fig. 16a).

The importance of deep-mantle contributions to free-air gravity anomalies is stronger than in the case of dynamic surface topography. The tomography-based mantle flow model reveals that gravity anomalies generated by density anomalies below 400 km depth (Fig. 16d) yield an rms amplitude that is 145% larger than the gravity signal generated by density anomalies in the upper 400 km of the mantle

(Fig. 16c). High-pass filtered free-air gravity anomalies have reduced contributions from density anomalies below 400 km depth, where the strength of reduction depends on the cut-off assumed for the longest wavelengths included in the gravity anomalies. If gravity anomaly contributions described by harmonic degrees 2 and 3 are removed (whose minimum wavelength is ~11,500 km), the rms amplitude of the gravity signal generated by density anomalies below 400 km depth (Fig. 16e) exceeds by over 100% the signal generated by all density anomalies in the upper 400 km of the mantle (Fig. 16c). If a stronger filtering is applied (e.g. Afonso et al. 2019), removing all contributions described by harmonic degrees 2 to 9 (minimum wavelength is ~4,200 km), the amplitude of the gravity anomalies due to density anomalies below 400 km depth is over 50% of the total signal in Fig. 16c. We finally note that a purely isostatic calculation of free-air gravity anomalies due to density anomalies in the top 400 km of the mantle (Fig. 16h, red curve) strongly misfits the data, yielding a variance reduction of -43% (up to harmonic degree 32), largely because the amplitude of the short wavelength components ($\ell > 10$) is too large, and the spatial correlation of the long wavelength components ($\ell < 10$) are too low (Fig. B1, Appendix B).

It is thus clear from the calculations discussed above, that recent efforts to model surface topography and gravity anomalies only in terms of shallow-mantle isostatic heterogeneity, will be significantly biased by "un-modelled" density anomalies in the deeper mantle. Appendix B presents a further detailed discussion of the implications of assuming isostasy on predicted topography and gravity anomalies, in particular the difficulties that emerge when the thickness of the shallow-mantle layer is greater than 200 km.

Figure 16 Here

Figure 16. Shallow- versus deep-mantle contributions to surface dynamic topography and free-air gravity anomalies, determined by a tomography-based mantle flow model (Lu et al. 2020) and radial viscosity profile derived by Mitrovica and Forte (2004). ***(a)*** *Dynamic topography generated by all density anomalies in a 400km-thick layer at the top of the mantle. All density anomalies below 400 km depth are set to zero.* ***(b)*** *The converse of (a), in which only density anomalies below 400 km depth are used to predict the dynamic surface topography.* ***(c)*** *and* ***(d)*** *are the predicted free-air gravity anomalies calculated as in (a) and (b), respectively.* ***(e)*** *Free-air gravity anomalies generated by all density anomalies below 400 km depth, where the longest-wavelength contributions corresponding to spherical harmonic degrees $\ell = 2, 3$ are removed. Same contour scale used as in (c) and (d).* ***(f)*** *The difference between the isostatic and dynamic surface topography, calculated using density anomalies in the top 400 km of the mantle only. All topography and gravity fields are represented by a spherical harmonic expansion truncated at degree $\ell = 32$.* ***(g)*** *Amplitude*

spectrum of dynamic topography predictions, defined as the root-mean-square amplitude at each spherical harmonic degree ℓ. The isostatic topography (red curve), calculated using density anomalies in the top 400 km of the mantle, is described in detail in Appendix B. ***(h)*** *Amplitude spectrum of the free-air gravity anomaly predictions, The details of the calculation of the isostatic free-air anomalies (red curve) is presented in Appendix B.*

Correlation of Dynamic Topography with Plate Boundaries

If one adopts the prevailing view that subducting slabs drive plate motions (Elsasser 1969, Richter 1973, Forsyth and Uyeda 1975, Richter 1977), and innumerable more recent assessments), and hence that ridges are entirely passive, then it follows there will be a predominant, hemispheric-scale correlation of dynamic topography lows with sinking slabs in the transition zone and lower mantle, as discussed above. However, an array of observations and modeling results raise significant questions as to the validity of this view.

(Rowley, Forte et al. 2016, Rowley and Forte 2022) document plate-kinematic observations that show the behavior of the East Pacific Rise is incompatible with models of Pacific plate motions driven by slab pull alone. Instead, active mantle-wide flow driven by an elongated linear (longitude-parallel) upwelling arises naturally out of best estimates of the buoyancy distribution in the mantle derived by joint seismic-geodynamic tomography inversions (Simmons et al. 2010, Forte et al. 2015, Lu et al. 2020), yielding predicted plate velocities that match the observations (Glišović and Forte 2014, Rowley, Forte et al. 2016). This is a major departure from the dominant perspective in which subducted-slab heterogeneity is the main, if not sole, driver of mantle convection dynamics. In the following we therefore review the principal underpinnings of this paradigm, leading to a reassessment of the relationship between plate boundaries and dynamic topography.

Slab-pull as the dominant driver of plate motions was predicated on: (1) two-layer convection in which the upper mantle above ~670 km was convecting separately from the lower mantle; and (2) negligible core mantle boundary (CMB) heat flux, relative to the top-of-mantle heat flux. These predicates were originally developed in the absence of seismic tomographic data that constrain the three-dimensional distribution of buoyancy within the mantle. Two-layer convection clearly decouples the realm of plates from any buoyancy arising from the CMB heat flux. As shown by (Richter and Parsons 1975) one of the important consequences of having a thin upper-mantle layer of convection, in which the layer thickness is small compared to horizontal dimensions of plates is the development of secondary, small-scale convection cells, now called Richter Rolls, that are characterized by rolls elongated in the direction of plate motions in which the convective flow is orthogonal to the direction of plate motions. Obviously, if Richter Rolls are present beneath plates then basal tractions cannot contribute to driving plate motions, thereby emphasizing, by default, the need for slab-driven plate kinematics.

The early assumption of independent upper and lower mantle convective systems, which predominated in the plate tectonic and geodynamic literature until the 1990s, was undermined by the work of Grand (Grand 1994) and (Grand, Van Der Hilst et al. 1997) in which the continuation of the Farallon slab beneath eastern North America into the mid-mantle was clearly imaged tomographically. Subsequent tomographic models, with the exception of stagnant slabs under the Honshu and Bonin trenches (e.g. (Fukao and Obayashi 2013), reveal that slabs generally penetrate through the lower mantle and thus this is a general property of Earth's convective system. A simple consequence of this realization is that the vertical and horizontal scales of convection (~1000s km) are comparable, thereby removing the argument (originally based on Richter Rolls) against basal tractions as an important driver of plate motions.

Sluggish convection in the lower mantle, independent of the upper-mantle, was entirely compatible with early estimates of very low CMB heat flux, in which relatively small (hotspot-related) plumes were assumed responsible for extracting the majority of the CMB heat flux. For example, (Sleep 1990) estimated that hotspot plume-related heat flux is approximately 2 TW. However, more recent estimates of CMB heat flux have significantly increased into the range of 10 to 20 TW (de Koker, Steinle-Neumann et al. 2012, Pozzo, Davies et al. 2012, Frost, Avery et al. 2022, Pozzo, Davies et al. 2022). Current estimates of top-of-mantle heat flux of ~40 TW (Jaupart, Labrosse et al. 2007, Lay, Hernlund et al. 2008) indicate that somewhere between 25% and 50% of this heat flux is coming from the core, having been extracted by mantle convection (Glišović, Forte et al. 2012, Glišović and Forte 2014). This augmented contribution from CMB heat flux accords with the finding that good fits to both seismic and geodynamic global data using mantle flow models require that about 50% of the buoyancy driving mantle convection and hence plate motions derive from active upwellings originating in the lowermost mantle and ~50% from the top of the mantle (slabs) (Rowley, Forte et al. 2016).

These recent developments reveal that at least some mid-oceanic ridges are not passive, in particular the East Pacific Rise, which has been Earth's dominant ridge over at least the past 80 Ma (Rowley, Forte et al. 2016), and also segments of the Mid-Atlantic Ridge. These findings thus suggest that a correlation between large scale mantle flow and resulting dynamic topography at divergent plate boundaries is expected, as is evident in Figures 13a, f and 16a, and particularly 16b but absent from most other assessments of dynamic topography as shown by the other panels in Fig. 13. This also contradicts the recent suggestion by Wang et al. (2022) that ridges are isostatically supported.

Broader Implications for Earth's Topography and its Change over time

The most obvious aspect of Earth's topography is the bimodal structure of its differential hypsometry (Fig. 5), where ocean basins are about 4 km deeper than continents. This bimodality primarily reflects the difference in thickness of the oceanic and continental crust modulated by crustal density, and which is significantly impacted by dynamic topography. The mean thickness of the oceanic crust is mainly set by mean mantle potential temperature (Klein and Langmuir 1987, McKenzie and Bickle 1988, Behn and Grove 2015) whereas the continental crust reflects a complex array of processes operating over protracted time scales that integrate to control its mean thickness (Rudnick and Gao 2014). A discussion of these is beyond the scope of the present paper. However, it is important to recognize that this bimodality provides the fundamental framework upon which secular changes in crustal isostatic and dynamic topography operate. The bimodality of crustal isostatic topography, relative to observed topography, is characterized by a significantly greater (~7 km) amplitude of the difference in elevation of oceanic and continental components (Fig. 5). The reduced amplitude of the observed differential hypsometry between the shallow and deep modes reflects the direct contribution of dynamic topography operating on different time scales (Forte, Peltier et al. 1993). On the longest time scales, the generally long residence time (>500 MY) of relatively dense continental lithospheric mantle depresses continental crust maintaining its mode at, or very near, sea level. The zero integral constraint (eq. 16), irrespective of the crustal model employed, requires that the negative dynamic topography of the continental crustal regions must be offset by positive dynamic topography in the oceans. Because mean oceanic lithosphere residence times are much shorter (<100 MY) than continental lithosphere mantle residence times the compensating oceanic dynamic topography must be continuously generated. This highlights that these components are coupled on the one hand but operate on completely different time scales. This coupling of isostatic and dynamic topography is completely compatible with the continuous operation of plate tectonics since the Archean or before. On shorter time scales dynamic topography is expected to have spatial and temporal variability with complex topographic consequences, and hence is expected to have had a significant impact on the geologic record as reflected in spatial and temporal variations in the stratigraphic record of the continents. Even small changes in mean age of the oceanic lithosphere, clearly a component of dynamic topography, can give rise to significant changes in continental flooding extent (Rowley, 2017).

It is likely that the depressed state of the continental crust is a very long-term feature of the Earth, reflective of the long residence time of continental crust, and strong coupling between the continental mantle lithosphere and the overlying crust, that therefore maintains this depressed height. Although there is much speculation as to the origins of the continental mantle lithosphere, based largely on mantle xenolith samples and much evidence of protracted alteration from what are presumed to be residual peridotites from partial melting (Pearson, Canil et al. 2014), our understanding of the evolution of this component of the Earth's mantle remains exceedingly limited. Joint seismic-geodynamic modelling (Forte and Perry 2000) has shown that although continental mantle lithosphere is chemically depleted resulting in positive compositional buoyancy, the negative thermal buoyancy due to colder temperatures is dominant to depths of about 250 km. Forte and Perry (2000, p. 1940) also note the "approximate equilibrium between thermal and chemical buoyancy contributes to cratonic stability over geological time." The significant thermal contribution to the negative buoyancy of continental mantle lithosphere, which dominates positive chemical buoyancy, was also revealed in joint seismic-geodynamic-mineral physical inversions (Simmons, Forte et al. 2010) and most recently at higher spatial resolution by (Lu, Forte et al. 2020) for a range of viscosity models.

There are several seismically imaged regions where thick lithospheric mantle is inferred to have existed in the past but is presently thinned. Recent petrological and seismic tomographic modelling of the African lithosphere (Celli, Lebedev et al. 2020) suggests significant mantle-plume-induced erosion or thinning of lithospheric roots below cratons over the past 200 Myr, particularly in northern Africa. This corresponds with the region responsible for the anomalous modal elevation at approximately +300m (Rowley, 2013) of Africa. In North America, the most robustly sampled region showing lithospheric thinning is the Colorado Plateau and eastern Great Basin region of the western United States (Schmandt and Lin 2014). The inference of the former extent of cratonic mantle lithosphere across this region is predicated on the regional Paleozoic and early Mesozoic stratigraphy characterized by relatively thin, predominantly shallow marine platform strata interfingering with coastal plain strata (Spencer 1996), comparable with sections farther east where cratonic mantle lithosphere is imaged today. Regions, both largely unaffected (i.e. the Colorado Plateau) and variably impacted by Basin and Range extension show significant dynamic topography reflecting, at least in part, the absence of this mantle lithospheric root. The correlation of Cenozoic uplift and absence of the mantle lithospheric root supports models where the mantle lithosphere contributes negative buoyancy to the cratons.

The long-term consequence of negatively buoyant continental lithosphere on topography is that the balance between crustal isostasy and this negative lithospheric buoyancy maintains continental crust at or near sea-level, thereby controlling continental freeboard. The net effect is that the dominant modal elevation of the solid Earth is at sea level (Rowley 2013), with global hypsometry graded to sea level (Fig. 5. The long-term persistence of this coupling explains the correlation of continental crustal heights with crustal thickness, as shown by (Ingalls, Rowley et al. 2016) and updated here using the GIA corrected topography (Fig. 17). Applying this relationship to compute the continental isostatic topography and differencing that from the observed topography yields a dynamic topography range from approximately -3.9 km to +3.3km with results quite comparable to that obtained using *Crust1.0*. It should be pointed out that the scaling of continental crustal thickness to elevation, with a value of 0.144, corresponds with $(\rho_m-\rho_c)/\rho_c$ and is not internally consistent with PREM mantle density and mean continental crustal density of *Crust1.0*, hence the conclusion that the dynamic topography of continents is depressed relative to isostasy is not contradicted by these results.

Figure 17 Here

Fig. 17. Relationship between crustal thickness of continental crust (Tcc) in Crust1.0 and elevation (Elev) using the GIA-corrected Etopo1. Horizontal uncertainties represent ±1s deviations of crustal thickness. Least squares regression and R^2 values also shown. Continental crust is here defined using a mask based on the (Müller, Dutkiewicz et al. 2013) age-grid, but excluding regions of arc-modified oceanic crust and accretionary prisms that are represented in the age grid as not oceanic crust.

One of the importamt aspects of this study is to highlight that the integral of dynamic topography over the surface of the Earth is zero (eq. 16). This topography includes the subsidence of oceanic lithosphere with age, which is the clearest signal in Earth's topography that the mantle is convecting, as emphasized earlier in the text. One of the profound consequences of this integral property is that changes in dynamic topography resulting from changes in, for example, the depth distribution of the oceanic crust, reflecting changes in the mean age of the oceanic lithosphere, are not independent of the height distribution of the continents (Rowley 2017). If at any time the mean depth of the ocean basins changes, then the mean height of the continents must necessarily change at the same time, to maintain a constant (globally averaged) mean elevation of the Earth. Thus, one cannot treat continental hypsometry independently from changes in ocean basin volume. This has important consequences for our understanding of long-term sea-level.

To illustrate the relationship between changes in mean depth of the oceans and corresponding changes in continental elevation we compare the geometrical/ hypsometric approach of Rowley (2017) with a dynamical model-based calculation of perturbations to the dynamic topography of the oceanic lithosphere. For present purposes we use GIA-corrected geography (Fig. 2) in which the depth of the oceans deeper than -3000m is perturbed by a fixed amount (+20 m), that tapers to 0 perturbation between -3000 m and -2600 m following the model of Rowley (2017) (Figure 18a). For reference a change of +20m corresponds a change in mean age of the oceanic lithosphere of ~-1.5 MY, using the depth-age model of Rowley (2018) to a mean age of ~61.7 Ma. For the dynamical calculation the mean depth perturbation is implemented by changing the thermal structure of the present oceanic lithosphere so as to match the geometrical perturbations mimicking a change in the mean age of the oceanic lithosphere and hence a change in dynamic topography of the oceanic lithosphere. The resulting global topography is computed using a spherical harmonic representation to degree 256 (Alex is this correct) by allowing the perturbed field to relax to equilibrium without imposing any constraints on the response of continental regions (Fig. 18b). The resulting global perturbation field is shown in Fig. 18c, and the corresponding, hypsometric comparison between the geometric/hypsometric approach and dynamical calculation is shown in Fig. 18d. Figure 18c makes clear that the response to a perturbation to the mean depth of the oceans gives rise to a global perturbation response, with the amplitude of opposite sign and larger amplitude over the continental regions. Figure 18 d shows two curves that are almost perfectly superimposed one computed by simply applying Rowley's (2017) geometric/hypsometric approach and the other the geodynamical approach. Figs. 18 b and d show the paleo-shoreline predicted by this perturbation field at ~57 m relative to present, with all ice treated as water. As modeled by Rowley (2017) and confirmed by Figures 18 b and d the areal extent of flooding correlates changes in ocean basin volume associated with changes in mean depth of the oceanic lithosphere.

Figure 18 Here

Fig. 18. Comparison of geodynamic and geometric/hypsometric approaches to changes in ocean basin volume associated with changes in the mean depth of the oceanic crust. a) Imposed perturbation field of oceanic depths of +20 m for depths <-3000 m, decreasing to 0m at -2600 m, elsewhere 0 m. b) Resulting global perturbation field of both continental and oceanic regions obeying the global integral equal zero constraint on changes in dynamic topography. c) Resulting global "paleogeography" with the paleo-shoreline highlighted by the black contour at +57 m. d) Hypsometric curves produced by the geometric/hypsometric approach of Rowley (2017) and geodynamic calculation – they are superimposed so indistinguishable, together with estimated paleo-shoreline height at +57 m, and areal extent of flooding derived by integrating ocean basin volume up to the volume of ocean water in the oceans plus all grounded ice as water. e) Comparison of modern Etopo1_ice hypsometry (gray), and 0Ma hypsometry (orange) and 300 Ma paleo-hypsometry (blue) curves both from Young et al. (2022, Fig. 8), where the 300 Ma paleohypsometry curve has been corrected by +130 m so that both 0 Ma and 300 Ma hypsometric curves share the same mean elevation.

Young et al. (2022) recently questioned Rowley's (2017) approach arguing that they do find a counter-balancing of oceanic and continental perturbations. The difference in their conclusion and that presented above is simple to explain. First, it is clear from their paleo-hypsometric curves that they do not actually enforce a constant global mean elevation. Examination of their Fig. 8 200 Ma, 300 Ma, and 400 Ma in which both the paleo-hypsometric and their modern curves are plotted. In each of these cases the paleo-hypsometric curve is significantly deeper in the oceans than their modern curve over regions of

~200*10^6 km^2 or greater. This is the same area as the above sea level parts of those curves, so, in order to maintain a constant mean elevation, the continental portions of their paleo-hypsometric curves would have to have the same mean difference but opposite sign as in the oceanic regions, which is clearly not the case. Second, they exclude depth-age within their definition of dynamic topography, and do not explicitly enforce that the global integral of variations in depth-age with age are also required to be equal to zero. The simple explanation for changes in mean elevation as shown by their Fig. 8 is that they allow changes in mean depth of the oceans to **not** be balanced by changes elsewhere. Hence, they have not included the global integral equals zero constraint for all components of their perturbation fields, which is what gives rise to the effect that they claim their analysis precludes. This last point can be shown by compelling their paleo-hypsometric curve, for example for their 300 Ma paleo-hypsometry to share the same mean elevation as their modern curve by correcting it upwards by ~130 m. Note that both curves were digitized from the same graph using the centers of each curve, thereby ensuring that they share the same scaling (Fig. 18e). When corrected for mean elevation differences the on average deeper oceans are balanced by higher continents, just as Rowley (2017) and the geodynamic analysis above requires. These points made above apply to previous treatments of this problem by Müller et al. (2008), and Wright et al. (2020) among others, resulting in increases and decreases in mean radius of the Earth on time scales of 10's of millions of years as discussed above. While not wanting to overly belabor the criticism of Young et al. (2022) it is worth noting on Fig. 18e that the thin gray curve represents the observed global hypsometry of Etopo1_ice (Amante and Eakins 2009). Comparing the observed (gray) and the orange curve that represents the Young et al. (2002) 0Ma hypsometry, it is clear these curves differ by ~500m in the deep oceans, such that the volume of water depicted on their Fig. 8 for 0 Ma is in fact more than 10% grater than actually is present based on Etopo1_Ice topography. For other intervals the implied volumes exceed modern values by more than 25% of ocean basin volume. In conclusion, Young et al. (2022) failure to replicate Rowley (2017) and our own geodynamic analys results from their failure to ensure that the global mean elevation remains constant. Using their paleo-hypsometry curves but enforcing a constant mean elevation replicates the results of Rowley (2017) and that presented above.

The framing of Earth's topography as the linear superposition of crustal isostatic topography and dynamic topography has important implications for understanding various aspects of the geologic record as exemplified by Figure 18b. It is not the purpose here to present model-based estimates of changes in isostatic or dynamic topography over time, but it is possible to derive important intuition regarding how changes in isostatic and dynamic topography manifest themselves in the geologic record. Perhaps the most obvious is in relation to the origins of accommodation reflected in the stratigraphic record of the continents. Changes in elevation of the surface at long wavelength relative to lithospheric flexure, have two drivers: generally local changes in crustal thickness and changes in dynamic topography. Changes in crustal thickness are primarily concentrated in regions of active tectonism, where crustal convergence and divergence result in thickening and thinning of the crust, respectively, which impact the isostatic topography. Similarly, erosion and deposition of sediments change local crustal thickness and isostatic topography, often tightly coupled with active tectonism.

Within a McKenzie (McKenzie 1978) extensional basin framework, the crustal isostatic response to stretching is crustal thinning and the production of localized rift basins, but the long-term subsidence is a response to dynamic topography induced by the cooling and thickening of the mantle lithosphere. Returning to the stratigraphic record of the nominally stable, undeforming parts of continents where crustal thickness was not changing, the vast majority of accommodation is the direct result of changes in dynamic topography, that is changes in mantle buoyancy associated with the large-scale flow of the mantle and perturbations to the thickness, thermal structure, and composition of the mantle lithosphere amplified by sediment loading. The stratigraphic record of the continents is therefore direct evidence for changes in dynamic topography as a function of time (e.g. Heine et al. 2008, Braun 2010)

It is important to keep in mind, as in discussions of GIA far-field effects from changes in ice and water loads whose global integral is zero, that analyses of the stratigraphic record must carefully distinguish proximal changes in dynamics and potential far-field influences as the mantle responds to satisfy the constraint that the global-average topography perturbation is zero (Fig. 18). For example, regions not significantly impacted by changes in crustal thickness, hence not expected to have significant variations in crustal isostatic height, such as the Colorado Plateau are nonetheless characterized by a kilometer and a half Paleozoic stratigraphic section in the Grand Canyon region of the southwestern United States exposed today at about a kilometer and a half of elevation. Neither the accommodation nor the current elevation would exist were it not for dynamic topography controlling these large amplitude changes in surface elevation. The sedimentary cover of the Colorado Plateau reflects the large-scale production of accommodation, amplified by water and sediment loading effects. However, is this stratigraphic record simply a consequence of local to regional perturbation or some combination of global changes in, for example, mean depth of the oceans, together with local changes due to differential motions of the mantle and overlying plates? At this time, it is not possible to answer these questions rigorously due to the inherent numerical difficulty in accurately backtracking the details of mantle flow on time scales longer than about 70 to perhaps 100 million years (e.g. (Bello, Coltice et al. 2014, Glišović and Forte 2014, Glišović and Forte 2016) while incorporating the full spectrum of dynamic topography that matches the definition of dynamic topography advocated here.

Conclusions

Earth's topography is most straightforwardly considered to be the result of the linear superposition of its crustal isostatic topography and dynamic topography. Crustal isostatic topography is the height of the surface due to the thickness and density of each column load relative to the sub-Moho mantle reference density, assuming the mantle is **not** convecting. Although there are uncertainties in the crustal thickness and density, this part of the Earth is better known and thus contributes less uncertainty than also including the mantle lithosphere in the isostatic component of Earth's topography. Explicit and implicit estimates of continental mantle lithosphere density vary greatly and thus should not be included in the "observed", i.e. isostatic part of Earth's topography. Including oceanic mantle lithospheric cooling related subsidence in the isostatic component of topography is inconsistent with the inherently dynamic origin of this topography, which would not exist in the absence of mantle convection. In addition, including this component adds an artificial step function change at COBs that adds an arbitrary constant deflection of the continents to compensate for the depth-age variations of the oceans, and that is not observed in residual topography estimates derived from differencing observed topography and crustal isostatic topography.

An isostatic ocean floor would be expected to be quite flat, reflecting the relative uniformity of oceanic crustal thickness and density (Fig. 3). Thus, the best estimate of oceanic isostasy also removes the lithosphere-age-dependent variation of water loading that reflects this convective contribution to ocean isostatic bathymetry, further flattening ocean isostatic topography. To be internally consistent, water-load corrections should only be applied to regions below the geoid and conserve the volume of water at the surface of the Earth. This requires iterative solution of the sea level equation with migrating shorelines. Continental crustal isostatic equilibrium, given current best estimates of thickness and density, as represented by Crust1.0, results in heights of the continents significantly higher than are observed today. A crude estimate of magnitudes of continental crustal thickness or density error required for the continents to actually be in isostatic equilibrium suggests that both thickness and density uncertainty are unlikely to account for the majority of non-isostatic topography.

A first order aspect of Earth's topography is its bimodality. This bimodality is underpinned by the bimodality in crustal thickness of the oceanic and continental crust. The amplitude of the difference in modes in the observed topography is approximately 4500m, whereas the amplitudes would be approximately 6700m were it controlled by crustal isostatic topography. Thus, Earth's bimodality is significantly impacted by dynamic topography, raising the ocean floor and lowering the continents. That Earth's observed topography is graded to sea level, and Earth's dominant mode is at sea level, supports the interpretation that this dynamic topographic contribution represents a long-term (>Ga) contributor to Earth's topography reflective of the lo the global integral of these perturbations ng-term stability of the continental mantle lithosphere. This obviates the criticism (Gurnis 1993) against linking oceanic depth-age subsidence with dynamic topography based on continental flooding histories. The continental crust is continually depressed because the continental mantle lithosphere and crust are coupled and have been on long time scales. Simultaneously, the decay of elevated mid-oceanic ridges associated with oceanic lithosphere age-depth subsidence is continuously generated offsetting negative continental dynamic topography thereby coupling short-time scale with long-term processes, compatible with long time-scale operation of plate tectonics.

Dynamic topography is the difference between the observed topography and the crustal isostatic topography. Dynamic topography quantifies the component of the observed topography that is not explained by crustal isostasy. One can subdivide the dynamic topography into various components, depth-age subsidence, continental mantle lithosphere contributions, mantle flow induced deflections, etc., but their sum must account for all of the non-crustal isostatic component of Earth's topography equal to what we explicitly refer to as dynamic topography.

An important aspect of dynamic topography is that its integral over the surface area of the Earth is zero. This implies that any subdivision of dynamic topography sources has to result in a global field that is required to satisfy this zero-integral constraint. As demonstrated in the joint seismic-geodynamic inversions by (Simmons, Forte et al. 2006, Simmons, Forte et al. 2009, Simmons, Forte et al. 2010, Lu, Forte et al. 2020) that solve for the distribution of seismic velocity and density with a complex viscosity structure, it is possible to explicitly solve for each of the contributions to fit observational estimates of Earth's dynamic surface topography. These models explicitly solve for the continental and oceanic lithospheric mantle contribution and all deeper-mantle contributions. These global joint tomography inversions thus provide explicit estimates of all of the components needed to account for the dynamic topography today.

The zero global integral constraint that applies to isostatic topography, glacial isostatic adjustment, and to dynamic topography has the important implication that local perturbations have global effects. A change to dynamic topography somewhere is not an isolated effect but is inherently coupled to responses everywhere. This is most obvious in discussions of long-term sea level controlled by changes in ocean basin volume. Since ocean basin volume is largely controlled by the mean depth of the oceanic lithosphere, which in turn is related to its mean age, variations in mean depth cannot be decoupled from continental elevation variations. If the mean depth of the oceans shallows, the mean height of the continents must decrease, and because the area of the oceans is greater than the continents the corresponding adjustment of the continents must be larger. The net result is that the large-scale flooding history of the continents can be accounted for by quite subtle variations in mean depth and hence mean age of the oceanic lithosphere.

We have suggested that dynamic topography is the major controller of the preserved stratigraphic record of the continents because this controls the vast majority of the production of accommodation on the continents. Local isostatic production of syn-rifting accommodation in rift basins, and relatively local flexural accommodation in thrust load basins are obvious exceptions, but virtually all other accommodation on the continents reflects the history of dynamic topography. Because of the zero global integral constraint, the radial position of every location on the Earth's surface must constantly adjust as Earth evolves. Thus, the height of any given location today may provide little or no insight into its elevation history. From this perspective, the Earth's surface acts like a 'magic carpet' with continental flooding variably reflecting local dynamics and far-field responses to changes in the global dynamic topography field as a function of time. Discerning the relative contributions of these near and far-field effects represents an important challenge for the future but has the potential to improve our understanding of the large-scale dynamical evolution of the Earth.

Acknowledgments

The order of authorship was determined by flip of a coin. The authors want to thank former fellows and members of the Canadian Institute for Advanced Research, Earth System Evolution Program for extensive discussions related to Earth's topography and its evolution. We want to thank Claudio Faccenna for the invitation to write this review. We thank Bernhard Steinberger for sharing grids related to his 2016 and 2019 papers and for his thoughtful review. AMF acknowledges funding from the University of Florida and from NSF grant EAR 1903108 for support of this work. AMF also acknowledges support from the French "*Programme d'investissements d'avenir*" under the auspices of the GYPTIS project – ANR 19 MPGA 0007. No external fund were used by DBR to support his contribution. DBR wants to acknowledge funds from Donald and Janet Rowley that supported aspects of this research. GIA corrected topography, Estimated and modelled residual and dynamic topography data are in the supplemental materials.

References

Afonso, J. C., Salajegheh, F., Szwillus, W., Ebbing, J. and C. Gaina (2019). "A global reference model of the lithosphere and upper mantle from joint inversion and analysis of multiple data sets." Geophysical Journal International **217**(3): 1602-1628.

Afonso, J. C., F. Salajegheh, W. Szwillus, J. Ebbing and C. Gaina (2019). "A global reference model of the lithosphere and upper mantle from joint inversion and analysis of multiple data sets." Geophysical Journal International **217**(3): 1602-1628.

Amante, C. and B. W. Eakins (2009). ETOPO1 1 Arc-Minute Global Relief Model: Procedures, Data Sources, and analysis. N. T. M. N. NGDC-24, U.S. Department of Commerce. **24:** 19.

Austermann, J. and J. X. Mitrovica (2015). "Calculating gravitationally self-consistent sea level changes driven by dynamic topography." Geophysical Journal International **203**(3): 1909-1922.

Backus, G. (1958). "A class of self-sustaining dissipative spherical dynamos." Annals of Physics **4**: 372-447.

Behn, M. D. and T. L. Grove (2015). "Melting systematics in mid-ocean ridge basalts: Application of a plagioclase-spinel melting model to global variations in major element chemistry and crustal thickness,." Journal of Geophysical Research **120**: 4863-4886.

Bello, L., N. Coltice, T. Rolf and P. J. Tackley (2014). "On the predictability limit of convection models of the Earth's mantle." Geochemistry, Geophysics, Geosystems **15**(6): 2319-2328.

Bird, P. (2003). "An updated digital model of plate boundaries." Geochemistry Geophysics Geosystems **4**: 52.

Braun, J. (2010). "The many surface expressions of mantle dynamics." Nature Geoscience **3**(12): 825-833.

Campbell, S. M., R. Moucha, L. A. Derry and M. E. Raymo (2018). "Effects of Dynamic Topography on the Cenozoic Carbonate Compensation Depth." Geochemistry, Geophysics, Geosystems **19**(4): 1025-1034.

Celli, N. L., S. Lebedev, A. J. Schaeffer and C. Gaina (2020). "African cratonic lithosphere carved by mantle plumes." Nat Commun **11**(1): 92.

Chambat, F. and B. Valette (2001). "Mean radius, mass, and inertia for reference Earth models." Physics of the Earth and Planetary Interiors **124**(3): 237-253.

Coffin, M. F. and O. Eldholm (1994). "Large igneous provinces: crustal structure, dimensions, and external consequences." Reviews of Geophysics **32**(1): 1-36.

Colli, L., S. Ghelichkhan and H. P. Bunge (2016). "On the ratio of dynamic topography and gravity anomalies in a dynamic Earth." Geophysical Research Letters **43**(6): 2510-2516.

Conrad, C. P. and L. Husson (2009). "Influence of dynamic topography on sea level and its rate of change." Lithosphere **1**(2): 110-120.

Crosby, A. G. and D. McKenzie (2009). "An analysis of young ocean depth, gravity and global residual topography." Geophysical Journal International **178**(3): 1198-1219.

de Koker, N., G. Steinle-Neumann and V. Vlcek (2012). "Electrical resistivity and thermal conductivity of liquid Fe alloys at high P and T, and heat flux in Earth's core." Proc Natl Acad Sci U S A **109**(11): 4070-4073.

Dziewonski, A. M. and D. L. Anderson (1981). "Preliminary reference Earth model." Physics of the Earth and Planetary Interiors **25**(4): 297-356.

Elsasser, W. M. (1969). Convection and stress propagation in the upper mantle. The application of modern physics to the Earth and planetary interiors. S. K. Runcorn. New York, Wiley-Interscience**:** 223-246.

Flament, N., M. Gurnis and R. D. Muller (2013). "A review of observations and models of dynamic topography." Lithosphere **5**(2): 189-210.

Forsyth, D. and S. Uyeda (1975). "Relative Importance of Driving Forces of Plate Motion." Geophysical Journal of the Royal Astronomical Society **43**(1): 163-200.

Forte, A. M. (2007). Constraints on Seismic Models from Other Disciplines, Implications for Mantle Dynamics and Composition. Treatise on Geophysics. G. Schubert. Amsterdam, Elsevier**:** 805-858.

Forte, A. M., R. Moucha, N. A. Simmons, S. P. Grand and J. X. Mitrovica (2010). "Deep-mantle contributions to the surface dynamics of the North American continent." Tectonophysics **481**(1-4): 3-15.

Forte, A. M., W. R. Peltier, A. M. Dziewonski and R. L. Woodward (1993). "Dynamic surface topography - A new interpretation based upon mantle flow models derived from seismic tomography." Geophysical Research Letters **29**: 225-228.

Forte, A. M., W. R. Peltier, A. M. Dziewonski and R. L. Woodward (1993). "Reply to comment by Gurnis." Geophysical Research Letters **20**(15): 1665-1666.

Forte, A. M. and H. Perry (2000). "Geodynamic Evidence for a Chemically Depleted Continental Tectosphere." Science **290**(5498): 1940-1944.

Forte, A. M., S. Quéré, R. Moucha, N. A. Simmons, S. P. Grand, J. X. Mitrovica and D. B. Rowley (2010). "Joint seismic–geodynamic-mineral physical modelling of African geodynamics: A reconciliation of deep-mantle convection with surface geophysical constraints." Earth And Planetary Science Letters **295**(3-4): 329-341.

Forte, A. M., N. A. Simmons and S. P. Grand (2015). Constraints on Seismic Models from Other Disciplines - Constraints on 3-D Seismic Models from Global Geodynamic Observables: Implications for the Global Mantle Convective Flow**:** 853-907.

Frost, D. A., M. S. Avery, B. A. Buffett, B. A. Chidester, J. Deng, S. M. Dorfman, Z. Li, L. Liu, M. Lv and J. F. Martin (2022). "Multidisciplinary Constraints on the Thermal-Chemical Boundary Between Earth's Core and Mantle." Geochemistry, Geophysics, Geosystems **23**(3).

Fukao, Y. and M. Obayashi (2013). "Subducted slabs stagnant above, penetrating through, and trapped below the 660 km discontinuity." Journal of Geophysical Research: Solid Earth **118**(11): 5920-5938.

Fullea, J., S. Lebedev, Z. Martinec and N. L. Celli (2021). "WINTERC-G: mapping the upper mantle thermochemical heterogeneity from coupled geophysical–petrological inversion of seismic waveforms, heat flow, surface elevation and gravity satellite data." Geophysical Journal International **226**(1): 146-191.

Glišović, P. and A. Forte (2016). "A new back-and-forth iterative method for time-reversed convection modeling: Implications for the Cenozoic evolution of 3-D structure and dynamics of the mantle." Journal of Geophysical Research: Solid Earth **121**: 4067-4084.

Glišović, P. and A. M. Forte (2014). "Reconstructing the Cenozoic evolution of the mantle: Implications for mantle plume dynamics under the Pacific and Indian plates." Earth and Planetary Science Letters **390**: 146-156.

Glišović, P., A. M. Forte and R. Moucha (2012). "Time-dependent convection models of mantle thermal structure constrained by seismic tomography and geodynamics: implications for mantle plume dynamics and CMB heat flux." Geophysical Journal International **190**(2): 785-815.

Glišović, P., S. P. Grand, C. Lu, A. M. Forte and S. S. Wei (2022). "The Effects of Discontinuity Topography in the Mantle Transition Zone on Global Geodynamic Observables and Mantle Heterogeneity." Geophysical Journal International **ggac074**.

Grand, S. P. (1994). "Mantle shear structure beneath the Americas and surrounding oceans." Journal of Geophysical Research: Solid Earth **99**(B6): 11591-11621.

Grand, S. P., R. D. Van Der Hilst and S. Widiyantoro (1997). "Global Seismic Tomography: A Snapshot of Convection in the Earth." GSA Today **7**(4): 1-7.

Gurnis, M. (1993). "Comment On "Dynamic Surface Topography: A New Interpretation Based Upon Mantle Flow Models Derived From Seismic Tomography"; By A.M. Forte, W. R. Peltier, A.M. Dziewonski And R. L. Woodward." Geophysical Research Letters **20**(15): 1663-1664.

Hager, B. H. and R. O'Connell (1981). "A simple global model of plate dynamics and mantle convection." Journal of Geophysical Research **86**: 4843-4867.

Herzberg, C., K. Condie and J. Korenaga (2010). "Thermal history of the Earth and its petrological expression." Earth and Planetary Science Letters **292**(1-2): 79-88.

Hoggard, M. J., J. Winterbourne, K. Czarnota and N. White (2017). "Oceanic residual depth measurements, the plate cooling model, and global dynamic topography." Journal of Geophysical Research: Solid Earth.

Ingalls, M., D. B. Rowley, B. Currie and A. S. Colman (2016). "Large-scale subduction of continental crust implied by India–Asia mass-balance calculation." Nature Geoscience **9**: 848-853.

Jarvis , G. and D. McKenzie (1980). "Convection in a compressive fluid with infinite Prandtl number." Journal of Fluid Mechanics **96**: 515-583.

Jaupart, C., S. Labrosse and J.-C. Mareschal (2007). Temperatures, Heat and Energy in the Mantle of the Earth. Treatise on Geophysics, vol. 7: Mantle dynamics. D. Bercovici and G. Schubert, Elsevier. **7:** 253-303.

Jordan, T. H. (1975). "The continental lithosphere." Reviews of Geophysics and Space Physics **13**(3): 1-12.

Jordan, T. H. (1988). "Structure and Formation of the Continental Tectosphere." Journal Of Petrology **Special Lithosphere Issue**: 11-37.

Kaban, M. K., P. Schwintzer, I. M. Artemieva and W. D. Mooney (2003). "Density of the continental roots: compositional and thermal contributions." Earth and Planetary Science Letters **209**(1-2): 53-69.

Klein, E. M. and C. H. Langmuir (1987). "Global correlations of ocean ridge basalt chemistry with axial depth and crustal thickness." Journal of Geophysical Research **92**(B8): 8089.

Korenaga, J. (2008). "Urey ratio and the structure and evolution of Earth's mantle." Reviews of Geophysics **46**(2).

Korenaga, T. and J. Korenaga (2008). "Subsidence of normal oceanic lithosphere, apparent thermal expansivity, and seafloor flattening." Earth and Planetary Science Letters **268**(1-2): 41-51.

Kustowski, B., G. Ekstrom and A. M. Dziewonski (2008). "Anisotropic shear-wave velocity structure of the Earth's mantle: A global model." Journal of Geophysical Research **113**(B6).

Laske, G., G. Masters, Z. Ma and M. Pasyanos (2013). Update on CRUST1.0 - A 1-degree Global Model of Earth's Crust. European Geophysical Union. Vienna, Geophysical Research Abstracts **15:** Abstract EGU2013-2658.

Lay, T., J. Hernlund and B. A. Buffett (2008). "Core–mantle boundary heat flow." Nature Geoscience **1**(1): 25-32.

Lu, C., A. M. Forte, N. A. Simmons, S. P. Grand, M. N. Kajan, H. Lai and E. J. Garnero (2020). "The Sensitivity of Joint Inversions of Seismic and Geodynamic Data to Mantle Viscosity." Geochemistry, Geophysics, Geosystems **21**(4).

McKenzie, D. (1977). "Surface deformation, gravity anomalies and convection." Geophysical Journal of the Royal Astronomical Society **48**: 211-138.

McKenzie, D. and M. Bickle (1988). "The volume and composition of melt generated by extension of the lithosphere." Journal of Petrology **29**: 625-679.

McKenzie, D. P. (1978). "Some remarks on the development of sedimentary basins." Earth and Planetary Science Letters **40**: 25-32.

Mitrovica, J. X. and A. M. Forte (2004). "A new inference of mantle viscosity based upon joint inversion of convection and glacial isostatic adjustment data." Earth And Planetary Science Letters **225**(1-2): 177-189.

Molnar, P., P. C. England and C. H. Jones (2015). "Mantle dynamics, isostasy, and the support of high terrain." Journal of Geophysical Research: Solid Earth **120**(3): 1932-1957.

Mooney, W. D., G. Laske and T. G. Masters (1998). "CRUST 5.1: A global crustal model at 5° × 5°." Journal of Geophysical Research: Solid Earth **103**(B1): 727-747.

Moritz, H. (2000). "Geodetic reference system 1980." Journal of Geodesy **74**(1): 128-162.

Moucha, R., A. M. Forte, J. X. Mitrovica and A. Daradich (2007). "Lateral variations in mantle rheology: implications for convection related surface observables and inferred viscosity models." Geophysical Journal International **169**(1): 113-135.

Müller, R., W. Roest, J. Royer, L. Gahagan and J. Sclater (1997). "Digital isochrons of the world's ocean floor." Journal Of Geophysical Research-Solid Earth **102**: 3211-3214.

Müller, R. D., A. Dutkiewicz, M. Seton and C. Gaina (2013). "Seawater chemistry driven by supercontinent assembly, breakup, and dispersal." Geology **41**(8): 907-910.

Müller, R. D., M. Sdrolias, C. Gaina, B. Steinberger and C. Heine (2008). "Long-Term Sea-Level Fluctuations Driven by Ocean Basin Dynamics." Science **319**(5868): 1357-1362.

Müller, R. D., M. Seton, S. Zahirovic, S. E. Williams, K. J. Matthews, N. M. Wright, G. E. Shephard, K. T. Maloney, N. Barnett-Moore, M. Hosseinpour, D. J. Bower and J. Cannon (2016). Ocean Basin Evolution and Global-Scale Plate Reorganization Events Since Pangea Breakup. Annual Review of Earth and Planetary Sciences. **44:** 107.

Pari, G. and W. R. Peltier (2000). "Subcontinental mantle dynamics: A further analysis based on the joint constraints of dynamic surface topography and free-air graviy." Journal of Geophysical Research: Solid Earth **105**(B3): 5635-5662.

Parsons, B. and J. Sclater (1977). "An analysis of the variation of ocean floor bathymetry and heat flow with age." Journal of Geophysical Research **82**(5): 803-827.

Pearson, D. G., D. Canil and S. B. Shirey (2014). Mantle Samples Included in Volcanic Rocks. Treatise on Geochemistry**:** 169-253.

Peltier, W. R. (1974). "The impulse response of a Maxwell Earth." Reviews of Geophysics **12**(4): 649-669.

Pitman, W. C., III (1978). "Relationship between eustacy and stratigraphic sequences of passive margins." Geological Society of America Bulletin **89**: 1389-1403.

Pozzo, M., C. Davies, D. Gubbins and D. Alfè (2012). "Thermal and electrical conductivity of iron at Earth's core conditions." Nature **485**: 355-358.

Pozzo, M., C. J. Davies and D. Alfè (2022). "Towards reconciling experimental and computational determinations of Earth's core thermal conductivity." Earth and Planetary Science Letters **584**.

Raymo, M. E., J. X. Mitrovica, M. J. O'leary, R. M. Deconto and P. J. Hearty (2011). "Departures from eustasy in Pliocene sea-level records." Nature Geoscience **4**(5): 328-332.

Richards, M. and B. H. Hager (1984). "Geoid anomalies in a dynamic Earth." Journal of Geophysical Research **89**: 5987-6002.

Richter, F. M. (1973). "Dynamical models for sea floor spreading." Reviews of Geophysics **11**(2): 223-287.

Richter, F. M. (1977). "Driving Mechanism of Plate Tectonics." Tectonophysics **38**: 61-88.

Richter, F. M. and B. Parsons (1975). "On the interaction of two scales of convection in the mantle." Journal of Geophysical Research **80**(17): 2529-2541.

Ritsema, J., H. J. van Heijst and J. H. Woodhouse (2004). "Global transition zone tomography." Journal of Geophysical Research **109**.

Rowley, D. B. (2013). "Sea Level: Earth’s Dominant Elevation—Implications for Duration and Magnitudes of Sea Level Variations." The Journal of Geology **121**(5): 445-454.

Rowley, D. B. (2017). "Earth’s Constant Mean Elevation: Implication for Long-Term Sea Level and Ocean Lithosphere Dynamics in a Pitman World." Journal of Geology **125**: 141-153.

Rowley, D. B. (2018). "Oceanic axial depth and age-depth distribution of oceanic lithosphere: Comparison of magnetic anomaly picks versus age-grid models." Lithosphere **11**(1): 21-43.

Rowley, D. B. and A. M. Forte (2022). "Kinematics of the East Pacific Rise Retrodicted From Pacific and Farallon/Nazca Subduction-Related Torques: Support for Significant Deep Mantle Buoyancy Controlling EPR Spreading." Journal of Geophysical Research: Solid Earth **127**(2).

Rowley, D. B., A. M. Forte, R. Moucha, J. X. Mitrovica, N. A. Simmons and S. P. Grand (2013). "Dynamic topography change of the eastern United States since 3 million years ago." Science **340**(6140): 1560-1563.

Rowley, D. B., A. M. Forte, C. J. Rowan, P. Glišović, R. Moucha, S. P. Grand and N. A. Simmons (2016). "Kinematics and dynamics of the East Pacific Rise linked to a stable, deep-mantle upwelling." Science Advances **2**(12).

Rudnick, R. L. and S. Gao (2014). "Composition of the Continental Crust." 1-51.

Schmandt, B. and F.-C. Lin (2014). "P and S wave tomography of the mantle beneath the United States." Geophysical Research Letters **41**(18): 6342-6349.

Seton, M., J. M. Whittaker, P. Wessel, R. D. Müller, C. DeMets, S. Merkouriev, S. Cande, C. Gaina, G. Eagles, R. Granot, J. Stock, N. Wright and S. E. Williams (2014). "Community infrastructure and repository for marine magnetic identifications." Geochemistry, Geophysics, Geosystems **15**(4): 1629-1641.

Simmons, N., A. Forte and S. Grand (2006). "Constraining mantle flow with seismic and geodynamic data: A joint approach." Earth And Planetary Science Letters **246**(1-2): 109-124.

Simmons, N. A., A. M. Forte, L. Boschi and S. P. Grand (2010). "GyPSuM: A joint tomographic model of mantle density and seismic wave speeds." Journal Of Geophysical Research-Solid Earth **115**.

Simmons, N. A., A. M. Forte and S. P. Grand (2009). "Joint seismic, geodynamic and mineral physical constraints on three-dimensional mantle heterogeneity: Implications for the relative importance of thermal versus compositional heterogeneity." Geophysical Journal International **177**(3): 1284-1304.

Sleep, N. H. (1990). " Hotspots and mantle plumes: some phenomenology." Journal of Geophysical Research **95**: 6715–6736.

Spasojevic, S. and M. Gurnis (2012). "Sea level and vertical motion of continents from dynamic earth models since the Late Cretaceous." AAPG Bulletin **96**(11): 2037-2064.

Spasojevic, S., M. Gurnis and R. Sutherland (2010). "Mantle upwellings above slab graveyards linked to the global geoid lows." Nature Geoscience **3**(6): 435-438.

Spencer, J. (1996). "Uplift of the Colorado Plateau due to lithosphere attenuation during laramide low-angle subduction." Journal Of Geophysical Research-Solid Earth **101**(B6): 13595-13609.
Stadler, G., M. Gurnis, C. Burstedde, L. C. Wilcox, L. Alisic and O. Ghattas (2010). "The Dynamics of Plate Tectonics and Mantle Flow: From Local to Global Scales." Science **329**(5995): 1033.
Stein, C. and S. Stein (1992). "A model for the global variation in oceanic depth and heat flow with lithospheric age." Nature **359**: 123-129.
Steinberger, B. (2007). "Effects of latent heat release at phase boundaries on flow in the Earth's mantle, phase boundary topography and dynamic topography at the Earth's surface." Physics of the Earth and Planetary Interiors **164**(1-2): 2-20.
Steinberger, B. (2016). "Topography caused by mantle density variations: observation-based estimates and models derived from tomography and lithosphere thickness." Geophysical Journal International **205**(1): 604-621.
Steinberger, B., C. P. Conrad, A. Osei Tutu and M. J. Hoggard (2019). "On the amplitude of dynamic topography at spherical harmonic degree two." Tectonophysics **760**: 221-228.
Szwillus, W., J. C. Afonso, J. Ebbing and W. D. Mooney (2019). "Global Crustal Thickness and Velocity Structure From Geostatistical Analysis of Seismic Data." Journal of Geophysical Research: Solid Earth **124**(2): 1626-1652.
Tapley, B., J. C. Ries, S. Bettadpur, D. Chambers, M. Cheng, F. Condi and S. Poole (2007). "The GGM03 mean Earth gravity model from GRACE." AGU Fall Meeting Abstracts **-1**: 03.
Wang, Y., L. Liu and Q. Zhou (2022). "Topography and gravity reveal denser cratonic lithospheric mantle than previously thought." Geophysical Research Letters **49**: e2021GL096844.
Weatherall, P., K. M. Marks, M. Jakobsson, T. Schmitt, S. Tani, J. E. Arndt, M. Rovere, D. Chayes, V. Ferrini and R. Wigley (2015). "A new digital bathymetric model of the world's oceans." Earth and Space Science **2**(8): 331-345.
Wright, N. M., M. Seton, S. E. Williams, J. M. Whittaker and R. D. Müller (2020). "Sea-level fluctuations driven by changes in global ocean basin volume following supercontinent break-up." Earth-Science Reviews **208**.
Yang, T. and M. Gurnis (2016). "Dynamic topography, gravity and the role of lateral viscosity variations from inversion of global mantle flow." Geophysical Journal International **207**(2): 1186-1202.
Young, A., N. Flament, S. E. Williams, A. Merdith, X. Cao and R. D. Müller (2022). "Long-term Phanerozoic sea level change from solid Earth processes." Earth and Planetary Science Letters **584**.

Appendix A: Change of Earth's mean radius due to secular cooling

We consider here the derivation of a general mathematical expression that may be used to quantify the change in Earth's mean (i.e. horizontally averaged) radius due to the slow secular cooling of Earth's interior. In the following, we assume a cooling time scale, $\Delta t \approx 10^9$ years, which is at least 3 orders of magnitude larger than the mantle-convection time scale ($\Delta t \approx 10^6$ years). We begin by considering (see Fig. A1) a small (cubical) mass dM that, at some (arbitrary) time, $t = t_0$, is located at position $\vec{r}$. At this time, the density of the mass element is ρ and it occupies as small volume $dV(t_0) = dxdydz$, such that

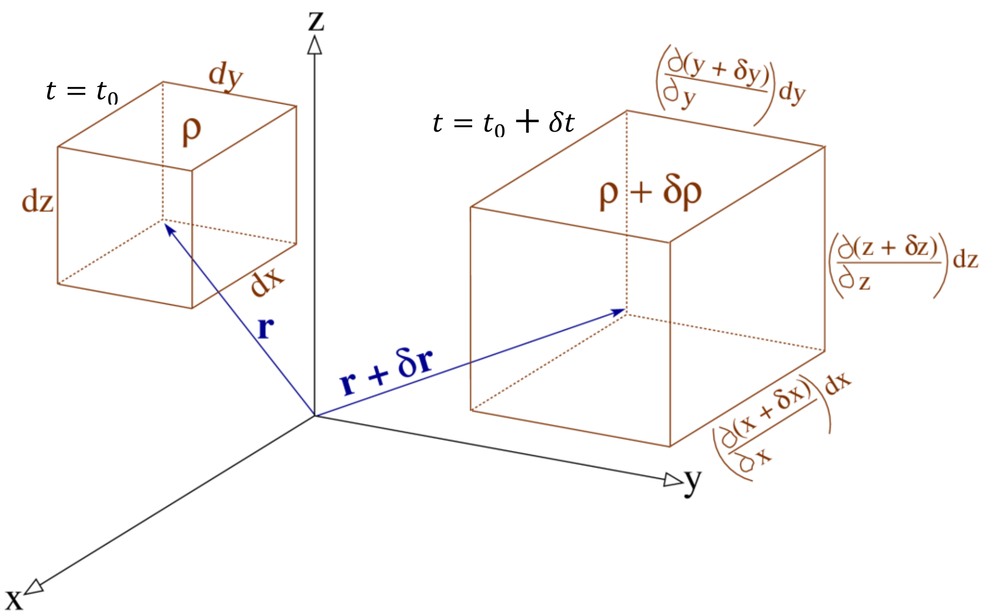

$dM(t_0) = \rho\, dV(t_0)$.

***Figure A1**. A schematic representation of a small mass element, whose initial ($t = t_0$), position and density are $\vec{r} = (x, y, z)$ and ρ, respectively. At a later time ($t = t_0 + \delta t$), the mass element is slightly displaced to position $\vec{r} + \delta\vec{r} = (x + \delta x, y + \delta y, z + \delta z)$ and its density will undergo a small perturbation $\rho + \delta\rho$. The initial volume is $dV(t_0) = dxdydz$ and the volume after the displacement is $dV(t_0 + \delta t) = \frac{\partial(x+\delta x)}{\partial x}\frac{\partial(y+\delta y)}{\partial y}\frac{\partial(z+\delta z)}{\partial z}\, dxdydz$.*

At some later time, $t = t_0 + \delta t$, the mass element will have experienced a small displacement and is located at position $\vec{r} + \delta\vec{r}$, and its density will have changed to $\rho + \delta\rho$ (Fig. A1). The displacement field is a continuous function of position and time, $\delta\vec{r} = \delta\vec{r}(\vec{r}, t)$ and it will be assumed that all changes are small, such that: $\|\delta\vec{r}/\vec{r}\| \ll 1$ and $|\delta\rho/\rho| \ll 1$. The displacement induces a volume change (Fig. A1): $dV(t_0 + \delta t) = \frac{\partial(x+\delta x)}{\partial x}\frac{\partial(y+\delta y)}{\partial y}\frac{\partial(z+\delta z)}{\partial z}\, dxdydz$, such that the mass is $dM(t_0 + \delta t) = (\rho + \delta\rho)dV(t_0 + \delta t)$. Mass conservation requires that:

$$dM(t_0) = dM(t_0 + \delta t) \;\Rightarrow\; \rho\, dxdydz = (\rho + \delta\rho)\, \frac{\partial(x+\delta x)}{\partial x}\, \frac{\partial(y+\delta y)}{\partial y}\, \frac{\partial(z+\delta z)}{\partial z}\, dxdydz \qquad \text{(A1)}$$

Assuming all perturbations (terms involving δ) are small, expression (A1) yields:

$$\left(1 + \frac{\delta\rho}{\rho} + \frac{\partial \delta x}{\partial x} + \frac{\partial \delta y}{\partial y} + \frac{\partial \delta z}{\partial z}\right) = 1$$

$$\Longrightarrow \qquad \vec{\nabla} \cdot \delta\vec{r} = -\,\frac{\delta\rho}{\rho} \qquad \text{(A2)}$$

where $\vec{\nabla}\cdot$ is the divergence operator. The Lagrangian or material time derivative of the displacement $\delta\vec{r}$ defines the velocity $\vec{v}$ of each mass element in the mantle:

$$\vec{v} = \frac{d}{dt}\,\vec{r} = \left(\frac{\partial}{\partial t}\right)_{\vec{r_0}} \delta\vec{r} = \left(\frac{\partial}{\partial t} + \vec{v}\cdot\vec{\nabla}\right)\vec{r} \qquad \text{(A3)}$$

where $\vec{r_0} = \vec{r}(t_0)$ is the initial position of each mass element, which is kept constant when calculating the material time derivative, and $\frac{\partial}{\partial t}$ is the Eulerian or local time derivative, at a <u>fixed</u> spatial location (e.g. *Malvern*, 1969). Therefore, the material time derivative, $\left(\frac{\partial}{\partial t}\right)_{\vec{r_0}}$, of both sides of equation (A2) yields:

$$\vec{\nabla}\cdot\vec{v} = -\frac{1}{\rho}\frac{d}{dt}\rho, \quad \text{where } \frac{d}{dt}\rho = \left(\frac{\partial}{\partial t}\right)_{\vec{r_0}} \delta\rho = \left(\frac{\partial}{\partial t} + \vec{v}\cdot\vec{\nabla}\right)\rho$$

$$\Leftrightarrow \; \frac{d}{dt}\rho + \rho\vec{\nabla}\cdot\vec{v} = 0 \;\Leftrightarrow\; \boxed{\frac{\partial\rho}{\partial t} + \vec{\nabla}\cdot\rho\vec{v} = 0} \qquad \text{(A4)}$$

The last expression in (A4) is the differential, time-dependent representation of the principle of mass conservation which is suited to fluid media (e.g. *Malvern*, 1969).

We revisited the mathematical derivation of this basic fluid-mechanical principle to underline the critical importance of the explicit modelling of the time derivative of density $\frac{\partial\rho}{\partial t}$, which is necessary for the accurate modelling of the time-dependent displacement field $\delta\vec{r}$ and hence, as we show below, the change of Earth's mean radius due to secular cooling. The current numerical models for mantle convection, notably *CitcomS* (*Zhong et al.*, 2008) and *ASPECT* (*Kronbichler et al.* 2012, *Heister et al. 2017*), assume either the Boussinesq approximation for mass conservation ($\vec{\nabla}\cdot\vec{v} = 0$) or the anelastic-liquid approximation ($\vec{\nabla}\cdot\rho\vec{v} = 0$). A recent critical evaluation of these approximations is presented by *Gassmöller et al.* (2020). Neither of these commonly used approximations will permit the correct modelling of changes in mean radius of the Earth, and of other internal boundaries. Indeed, the Boussinesq approximation necessarily leads to zero change of mean radius. Similarly, the most common implementation (e.g. in *CitcomS*) of the anelastic-liquid approximation ($\vec{\nabla} \cdot \rho_0(r)\,\vec{v} = 0$, where $\rho_0(r)$ is the reference radial density profile) must yield zero change of mean radius, as also shown in the main text (equation 16). The current mantle convection models must then be supplemented by an additional set of calculations for mean radius change that are presented below.

Returning to (A2), this expression is generally used to determine local density (hence local volume) perturbations that arise from a specified displacement field. In the following we proceed inversely and determine the displacement field $\delta\vec{r}$ corresponding to a specified perturbation of density $\delta\rho/\rho$. This determination is necessarily non-unique, since a single scalar input (density) cannot uniquely constrain all 3 components of the displacement vector. In the following, we explicitly identify the mathematical character of this non-uniqueness and then demonstrate its irrelevance when modelling changes in mean (horizontally averaged) radius of the Earth. We begin by first seeking the scalar function $f(\vec{r}, t)$ such that:

$$\vec{\nabla} \cdot f\hat{\mathrm{r}} = \frac{1}{r^2}\frac{\partial r^2 f}{\partial r} = -\,\frac{\delta\rho}{\rho} \qquad \text{(A5)}$$

$$\Longrightarrow \qquad f(r,\theta,\varphi,t) \;=-\frac{1}{r^2}\int_0^r \acute{r}^2\,\frac{\delta\rho}{\rho}(\acute{r},\theta,\varphi,t)\;d\acute{r} \qquad \text{(A6)}$$

where $\hat{\mathrm{r}}$ is the unit radial vector, and (r, θ, φ) are the radius, co-latitude and longitude in a spherical coordinate system. From expressions (A2-A3), we note the most general expression for the displacement field $\delta\vec{r}$ is:

$$\delta\vec{r} = f\hat{\mathrm{r}} + \delta\vec{r_s} \qquad \text{(A7)}$$

where $\overrightarrow{\delta r_s}$ must necessarily satisfy the condition:

$$\vec{\nabla} \cdot \delta\vec{r_s} = 0 \qquad \text{(A8)}$$

Equation (A8) shows that $\delta\vec{r_s}$ is an incompressible (solenoidal) displacement that produces no volume and hence no density changes. Its most general mathematical representation, following *Backus* (1958), is:

$$\delta\vec{r_s} = \vec{\nabla}\,\mathrm{x}\,\vec{\Lambda}\,\delta p + \vec{\Lambda}\,\delta q \quad , \qquad \text{(A9)}$$

where δp and δq are scalar potentials that represent the poloidal and toroidal components of the displacement, respectively, and $\vec{\Lambda} = \vec{r}\,\mathrm{x}\,\vec{\nabla}$, where $\vec{r}$ is the radial position vector. The right-hand side of equation (A9) can be rewritten as:

$$\delta\overrightarrow{r_s} = \hat{\mathrm{r}}\ \frac{\Lambda^2}{r}\delta p + \hat{\mathrm{r}}\ \mathrm{x}\ \vec{\Lambda}\left(\frac{1}{r}\frac{\partial\ r\delta p}{\partial r}\right) + \vec{\Lambda}\ \delta q \qquad \text{(A10)}$$

where $\hat{\mathrm{r}}$ is a unit radial vector and $\Lambda^2 = \vec{\Lambda}\cdot\vec{\Lambda}$ is the horizontal Laplacian operator. Both operators $\hat{\mathrm{r}}\ \mathrm{x}\ \vec{\Lambda} = \vec{\nabla}_H$, the horizontal gradient on a unit-radius sphere, and $\vec{\Lambda}$ describe only the horizontal components of $\delta\overrightarrow{r_s}$.

We now consider the purely radial component of the displacement $\delta\vec{r}$. From expressions (A6-A7) and (A10), we obtain:

$$\delta r(r,\theta,\varphi,t) = -\frac{1}{r^2}\int_0^r \acute{r}^2\ \frac{\delta\rho}{\rho}(\acute{r},\theta,\varphi,t)\ d\acute{r} + \frac{\Lambda^2}{r}\delta p \qquad \text{(A11)}$$

If we now calculate the global horizontal average of all terms in (A11), we finally obtain:

$$\boxed{\delta\bar{r}(r,t) = -\frac{1}{r^2}\int_0^r \acute{r}^2\ \frac{\overline{\delta\rho}}{\rho}(\acute{r},t)\ d\acute{r}} \qquad \text{(A12)}$$

where we use the notation $\bar{f}$ to represent the global average of a function f:

$$\bar{f}(r) = \frac{1}{4\pi}\oint_{S_1} f(r,\theta,\varphi)\ d^2S \qquad \text{(A13)}$$

where S_1 represents the surface of a unit-radius sphere. In arriving at (A12) we also employed the mathematical identity (*Backus* 1958):

$$\oint_{S_1} \Lambda^2 f\ d^2S = 0 \qquad \text{(A14)}$$

In (A11) we note that the poloidal contribution (δp) to the radial displacement is completely undetermined. Additional information is needed to uniquely constrain this laterally variable contribution to the radial displacement, which may arise from other mantle processes, if such processes lead to volume preserving (incompressible) displacements. The latter is not the case for mantle convection, where fluid motions are compressible.

The density perturbations $\delta\rho$, which occur over a secular-cooling time interval Δt, may be generated by changes in temperature (T), pressure (P), composition and/or phase (C):

$$\frac{\delta\rho}{\rho} = -\alpha\ \delta T + K^{-1}\delta P + \frac{1}{\rho}\left(\frac{\partial\rho}{\partial C}\right)\delta C \qquad \text{(A15)}$$

where α is the volume coefficient of thermal expansion and K is the incompressibility modulus, both of which are assumed (for mathematical convenience) to be functions of radius only. In the following, we focus only on the temperature- and pressure-induced changes to density associated with the secular cooling of the Earth and, in particular, their global horizontal averages (A13) that only depends on radius r:

$$\frac{\overline{\delta\rho}}{\rho}(r, t_0 + \Delta t) = -\alpha \; \overline{\delta T}(r, t_0 + \Delta t) \; + \; K^{-1} \, \overline{\delta P}(r, t_0 + \Delta t) \qquad \text{(A16)}$$

It is important to appreciate that in (A16), both $\overline{\delta T}$ and $\overline{\delta P}$ are small changes in the global mean temperature and pressure, which reflect the evolution (over a time interval Δt) of the average structure of the Earth due to secular cooling. If we assume that convection processes efficiently stir both the mantle and core, the mean radial structure in both regions will be close to adiabatic (excluding thermal boundary layers at the top and bottom of the mantle), and therefore an isentropic incompressibility modulus should be employed in (A16) for the bulk of the mantle and core: $K = K_s$. Substituting (A16) into (A12) and setting $r = r_e$, the Earth's external radius, yields:

$$\delta \overline{r_e} = \frac{1}{{r_e}^2} \int_0^{r_e} \acute{r}^2 \left(\alpha \; \overline{\delta T} - \; {K_s}^{-1} \, \overline{\delta P} \right) d\acute{r} \qquad \text{(A17)}$$

Expression (A17), ignoring the pressure contribution (${K_s}^{-1} \to 0$), is the same as that derived by *Jeffreys* (1929, p. 280) in his treatment of thermal contraction of the Earth. In this case, if we simply assume that the expansion coefficient and mean temperature change are approximately constant with depth, (A17) then yields:

$$\delta \overline{r_e} \approx r_e \, \frac{\alpha}{3} \, \overline{\delta T} \qquad \text{(A18)}$$

Secular cooling, $\overline{\delta T} \; < 0$, will thus lead to thermal contraction of Earth's mean radius: $\delta \overline{r_e} \; < 0$.

We now evaluate whether the change in mean pressure, $\overline{\delta P}$ in (A17), provides a significant contribution to the change of mean radius. To address this issue, we must consider how internal pressure (P), density (ρ) and gravity ($\vec{g}$) are maintained in balance with each other, via the coupled equations of hydrostatic equilibrium and gravitation (the differential form of Newton's law of gravity):

$$-\vec{\nabla} \mathrm{P} + \; \rho \vec{g} = 0$$

$$\vec{\nabla} \cdot \vec{g} = \; -4\pi \mathrm{G} \, \rho \qquad \text{(A19)}$$

where G is the universal constant of gravitation. *Jaupart et al.* (2007) provide an approximate solution to these coupled equations, assuming a purely radial Earth structure with an adiabatic temperature profile. Using their solution for the radial variation of global mean density and gravity, a straightforward integration (using the 1st equation in A19) yields the mean hydrostatic pressure field:

$$\bar{P}(r) = K_s\, \varepsilon \left\{ \frac{4\pi}{6}(1 - \tilde{r}^2) + \varepsilon\, \frac{(4\pi)^2}{90}[5(1-\tilde{r}^2) - 2(1-\tilde{r}^4)] \right\} \tag{A20}$$

$$\text{where } \tilde{r} = r/r_e \text{ and } \varepsilon = {K_s}^{-1} G\, \rho_0^2\, r_e^2 \,,$$

in which ρ_0 is the mean <u>surface</u> density. In *Jaupart et al.* (2007) the following values are employed: $K_s = 150\ GPa$ (assumed constant) and $\rho_0 = 3300\ kg/m^3$, which yield $\varepsilon = 0.2$. This choice of parameters does not yield a match to Earth's total mass, which is not unexpected given the simplified 1st-order modelling of $\bar{\rho}(r)$ by *Jaupart et al.* (2007), which also assumes constant K_s and does not include an explicit treatment of density in the metallic core. The total mass constraint can be satisfied by changing the value of the surface density to $\rho_0 = 4302\ kg/m^3$, assuming $K_s = 150\ GPa$, which yields $\varepsilon = 0.334$. Adopting this revised value in expression (A20) yields a mean pressure at the CMB ($\tilde{r} = 0.546$) $\overline{P_{CMB}} = 123\ GPa$, which compares reasonably well with $\overline{P_{CMB}} = 136\ GPa$ in PREM (Dziewonski and Anderson 1981).

Perturbations to the mean pressure, $\overline{\delta P}$, will arise when the mean density (and hence gravity) profile of the Earth changes in response to changes in mean temperature. This can be modelled, in the context of expression (A20), by perturbing ε as follows:

$$\delta\varepsilon = 2\varepsilon\left(\frac{\delta\rho_0}{\rho_0} + \frac{\delta r_e}{r_e}\right) \approx 2\varepsilon\left(-\alpha\overline{\delta T} + \frac{\alpha}{3}\,\overline{\delta T}\right) = -\varepsilon\,\frac{4}{3}\alpha\overline{\delta T} \tag{A21}$$

where we used approximation (A18) for $\delta r_e/r_e$, retaining only terms up to 1st order in ε (noting that ${K_s}^{-1}\,\overline{\delta P} \sim O(\varepsilon)$ as is evident in A20). Expressions (A20, A21) thus yield, to 1st order in ε:

$${K_s}^{-1}\,\overline{\delta P} \approx \delta\varepsilon \frac{4\pi}{6}\left(1 - \tilde{r}^2\right) = -\varepsilon\,\alpha\overline{\delta T}\,\frac{16\pi}{18}\left(1 - \tilde{r}^2\right) \tag{A22}$$

Substituting (A22) into (A17) finally yields:

$$\frac{\delta \bar{r}_e}{r_e} \approx \frac{\alpha}{3}\overline{\delta T}\,\left(1 + \varepsilon\frac{16\pi}{45}\right) \tag{A23}$$

which is identical to the expression for mean radius change that was obtained by *Jaupart et al.* (2007), who used a different approach involving consideration of the total mass of the Earth. Result (A23) thus demonstrates that gravity in conjunction with the finite compressibility of the mantle, both implying $\varepsilon > 0$, will enhance the contraction of mean radius due to secular cooling of the Earth. For the value $\varepsilon = 0.334$, which matches the total mass of the Earth, the enhancement is 37%.

Appendix B: Extending isostasy to the mantle – Implications for topography and gravity

Here we consider the implications of extending the concept of isostatic equilibrium, which was developed for the crust in expression (22), to a shallow heterogeneous layer within the underlying lithospheric mantle and asthenosphere. This formulation of isostasy will be based on the assumption that the lateral variations in density be confined to a shallow layer at the top of the mantle. Moreover, and most importantly, this formulation must satisfy the same key constraint that was applied to the crust: that all lateral variations in pressure below this shallow-mantle layer must vanish, thereby ensuring the maintenance of hydrostatic equilibrium in the underlying mantle. A critical examination of this requirement was presented in the main text (see Fig. 15 and associated discussion), where it was found that the condition of no horizontal pressure variations cannot be rigorously satisfied for a shallow layer within the viscous mantle. Indeed, it was found to be only approximately satisfied, depending on the thickness of the layer in question (see Table 1 in the main text). In the following we intentionally ignore this difficulty and again assume that classical isostasy can be applied to the mantle. The objective is to quantify the departure from fluid dynamical consistency and to consider the implications of assuming mantle isostasy for surface topography and gravity anomalies.

We begin by extending the isostatic equilibrium equation (22) to the shallow mantle. For simplicity we will treat the crust as mechanically coupled to and passively responding to the movements of the lithosphere. The crust + lithosphere will thus be treated as a single layer. From the PREM reference model (Dziewonski & Anderson 1981), the average density of the crust + lithosphere layer (yielding same total mass) is 3200 kg/m^3. Following equation (22), shallow-mantle isostasy may then be expressed by the following relation:

$$\delta P_{total} = \{\, \Delta\rho\, \delta r_s + \sigma_m - \overline{\sigma_m} \,\}\, g = 0$$

$$\text{where} \quad \sigma_m - \overline{\sigma_m} = \int_{r_m}^{r_s} \delta\rho\,(r,\theta,\varphi)\, dr \qquad \text{(B1)}$$

where $\Delta\rho$ is the density jump at the surface (air/water relative to average crust+lithosphere density), $\delta\rho(r,\theta,\varphi)$ are the lateral density variations in the shallow mantle layer whose bottom radius is r_m and whose surface radius (at the top of crust+lithosphere) is r_s, and $\delta r_s(\theta,\varphi)$ are the laterally variable undulations of the solid surface. In (B1), the global average of the lateral density variations $\delta\rho$ is zero, because they do not include the mean (horizontal average) density change associated with secular changes in the geotherm. The latter is handled separately, as described in Appendix A. This implies that the global average of the surface undulations δr_s must therefore vanish, implying no change in mean radius of the surface, in accord with expression (16) in the main text. We note here that the surface undulations δr_s due to heterogeneity in the shallow mantle coexist with, and are additive to, the surface undulations due to isostatically compensated crustal heterogeneity. Indeed, the isostatic requirement that there be no lateral pressure variations in the underlying mantle are satisfied when expressions (22) and (B1) are simultaneously satisfied. Strictly speaking, then, the radial integral of lateral density variations in (B1) extends only to the radius of the Moho: $r_m \leq r \leq r_{moho} (< r_s)$.

Expression (B1) then yields

$$\delta r_s(\theta, \varphi) = -\frac{1}{\Delta\rho} \int_{r_m}^{r_s} \delta\rho(r, \theta, \varphi)\, dr \tag{B2}$$

From (B2) we obtain the following relationship between the spherical harmonic coefficients of the mantle density anomalies and surface topography:

$$(\delta r_s)_\ell^m = -\frac{1}{\Delta\rho} \int_{r_m}^{r_s} \delta\rho_\ell^m(r)\; dr \tag{B3}$$

where ℓ, m are the harmonic degree and azimuthal order, respectively, of the corresponding spherical harmonic basis function $Y_\ell^m(\theta, \varphi)$ such that, in the case of the surface topography:

$$\delta r_s(\theta, \varphi) = \sum_{\ell=0}^{\infty} \sum_{m=-\ell}^{+\ell} (\delta r_s)_\ell^m \;\; Y_\ell^m(\theta, \varphi) \tag{B4}$$

and a similar harmonic expansion applies to the lateral density variations $\delta\rho(r, \theta, \varphi)$. A direct relationship exists between the harmonic degree ℓ and horizontal wavelength λ_ℓ that characterizes the spatial oscillations of the spherical harmonics:

$$\lambda_\ell = \frac{2\pi\, r}{\sqrt{\ell(\ell+1)}} \tag{B5}$$

where r is the radius of the surface in consideration (e.g. $r = r_s$).

We compare expression (B3) with the following general expression (e.g. Forte et al. 1993) for dynamic topography generated by density anomalies in a viscous, flowing mantle:

$$(\delta r_s)_\ell^m = \frac{1}{\Delta\rho}\int_{r_{cmb}}^{r_s} T_\ell(r)\,\delta\rho_\ell^m(r)\;dr \qquad \text{(B6)}$$

where $T_\ell(r)$ is a dynamic topography kernel that depends on radius, harmonic degree, and the rheological structure (i.e. viscosity) of the mantle. Comparing expressions (B3) and (B6), we conclude that the dynamic topography kernels for an <u>isostatic</u> shallow-mantle layer are simply

$$T_\ell^{iso}(r) = -1, \text{for } r > r_m \qquad \text{(B7)}$$

In other words, the isostatic topography kernels do not change with depth in the shallow-mantle layer (but vanish below it), nor do they change with horizontal wavelength λ_ℓ as defined in (B5). Finally, the isostatic kernels are not dependent on the viscosity structure of the mantle.

We next consider the perturbations to the gravitational potential, $\delta U(\theta,\varphi)$, due to the density anomalies in the shallow mantle layer, $\delta U_{int}(\theta,\varphi)$, plus the gravitational perturbation produced by the laterally variable vertical displacement of the surface, $\delta U_{top}(\theta,\varphi)$:

$$\delta U(\theta,\varphi) = \delta U_{int}(\theta,\varphi) + \delta U_{top}(\theta,\varphi) \;\Longrightarrow\; \delta U_\ell^m = (\delta U_{int})_\ell^m + (\delta U_{top})_\ell^m \qquad \text{(B8)}$$

The spherical harmonic coefficients of the potential perturbations due to the mantle density anomalies and the isostatic surface topography are, respectively, given by the following expressions (e.g. Forte & Peltier 1987):

$$(\delta U_{int})_\ell^m = \frac{4\pi\,G\,r_s}{2\ell+1}\int_{r_m}^{r_s}\left(\frac{r}{r_s}\right)^{\ell+2}\delta\rho_\ell^m(r)\,dr \;\text{ and }\; (\delta U_{top})_\ell^m = \frac{4\pi\,G\,r_s}{2\ell+1}\,\Delta\rho\,(\delta r_s)_\ell^m \qquad \text{(B9)}$$

Combining expressions (B3), (B8) and (B9) yields:

$$(\delta U)_\ell^m = \frac{4\pi\,G\,r_s}{2\ell+1}\int_{r_m}^{r_s}\left[\left(\frac{r}{r_s}\right)^{\ell+2} - 1\right]\delta\rho_\ell^m(r)\,dr \equiv (\delta U^{iso})_\ell^m \qquad \text{(B10)}$$

where the geopotential perturbation in (B10) is identified as an 'isostatic anomaly', δU^{iso}, since it incorporates an isostatic treatment for surface topography given by expression (B3). If, rather than radius, we employ depth $z = r_s - r$ and assume a thin layer, such that $(r_s - r_m)/r_s \ll 1$, expression (B10) can then be approximated as follows:

$$(\delta U^{iso})_\ell^m \approx 4\pi\, G \frac{\ell+2}{2\ell+1} \int_{z_m}^{0} z\, \delta\rho_\ell^m(z)\, dz \qquad \text{(B11)}$$

where $z_m = r_s - r_m$. In the limit of short horizontal wavelength, $\lambda_\ell \to 0$ corresponding to $\ell \to \infty$, (B11) yields the following expression for isostatic perturbations of the geoid, $\delta N = \delta U/g_0$ (g_0 is the mean surface gravitational acceleration):

$$(\delta N^{iso})_\ell^m = \frac{(\delta U^{iso})_\ell^m}{g_0} = \frac{2\pi\, G}{g_0} \int_{z_m}^{0} z\, \delta\rho_\ell^m(z)\, dz, \text{when } \ell \to \infty, \qquad \text{(B12)}$$

which is the classic short-wavelength expression for isostatic geoid anomalies on a flat Earth derived by Haxby & Turcotte (1978). Returning to (B10), the isostatic geoid anomalies may be expressed as follows:

$$(\delta N^{iso})_\ell^m = \frac{3}{2\ell+1} \frac{1}{\bar{\rho}} \int_{r_m}^{r_s} G_\ell^{iso}(r)\ \delta\rho_\ell^m(r)\, dr \ \text{ where } \ G_\ell^{iso}(r) = \left[\left(\frac{r}{r_s}\right)^{\ell+2} - 1\right] \qquad \text{(B13)}$$

where $\bar{\rho}$ is the average density of the Earth and $G_\ell^{iso}(r)$ are the isostatic geoid kernels. The free-air gravity anomalies, δG, may be obtained from the geoid anomalies, δN, using the following expression:

$$(\delta \mathrm{G})_\ell^m = \frac{g_0}{r_0}\, (\ell - 1)\, (\delta \mathrm{N})_\ell^m \qquad \text{(B14)}$$

where r_0 is the Earth's mean radius.

In Fig. B1 (panel a & b) we plot the isostatic topography and gravity kernels, $T_\ell(r)$ and $G_\ell(r)$ respectively, and compare them with 'dynamic' kernels for a viscous, compressible mantle in which the effects of self-gravitation are fully incorporated (Forte 2007). We note the isostatic kernels best match the viscous-flow kernels that assume a no-slip surface boundary condition, but the differences rapidly increase for depths greater than ~100 km. The isostatic kernels in (B7) and (B13) are then employed to predict isostatic topography and free-air gravity anomalies using mantle density anomalies given by the tomography model of (Lu, Forte et al. 2020). In this calculation, we consider two different thickness for the shallow-mantle layer: 200 and 400 km. The amplitude spectrum of the predicted topography and gravity fields (panel c & d in Fig. B1), shows that the density anomalies in a 400km-thick layer yield a fairly good match to the crust-corrected FR2021 dynamic topography amplitude (Fig. 7), especially for harmonic degrees $\ell > 4$, but the amplitude of the predicted gravity anomalies, for harmonic degrees $\ell > 9$, are too large compared to the data. A 200km-thick isostatic layer follows the trend of the amplitude spectrum of both the topography and gravity data, but the predicted amplitudes are systematically too small.

We finally consider the wavelength-dependent, spatial ('degree') correlations of the predicted isostatic topography and gravity anomalies with the corresponding data (panel e and f in Fig. B1). The correlations with the topography data are highly significant for harmonic degrees $\ell > 4$ for both the 200km- and 400km-thick shallow-mantle layers, albeit with a slow degradation in correlation as harmonic degree increases. In marked contrast, the correlations with the gravity data are poor for degrees $\ell < 12$, and strongly increase to highly significant levels at higher degrees ($\ell \geq 13$) for both the 200km- and 400km-thick mantle layers. We recall, however, that the 400km-thick isostatic layer yields spectral amplitudes that strongly exceed the gravity data when $\ell > 9$. In conclusion, it appears that a purely isostatic treatment of shallow-mantle heterogeneity yields surface topography predictions that match the data fairly well, but does not yield an adequate match to the free-air gravity data when the thickness of the shallow-mantle layer exceeds 200km, mainly due to the excessive amplitude of the gravity prediction (Fig. B1).

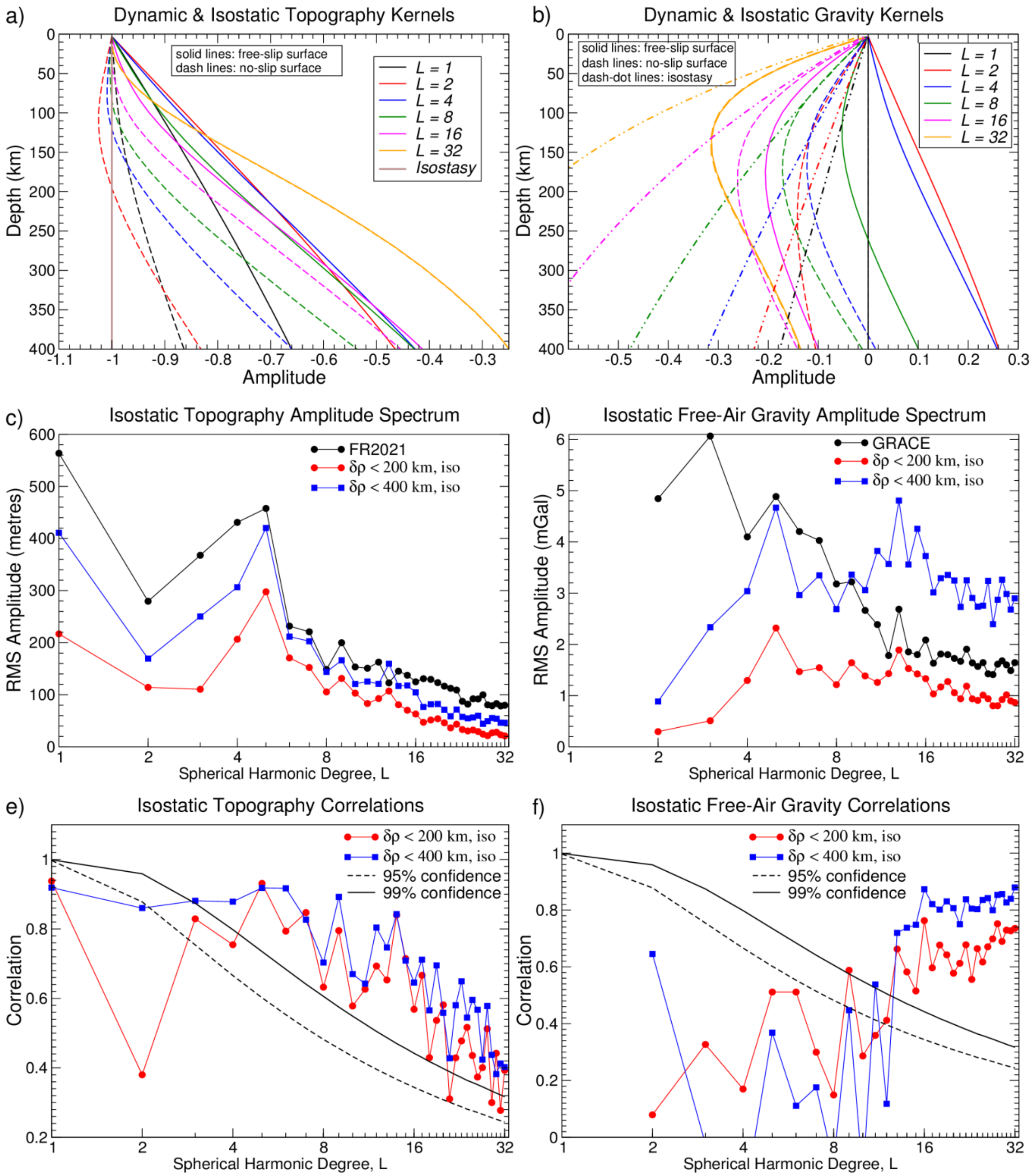

1988 ***Figure B1****. Modelling isostatic topography and free-air gravity anomalies.* ***(a)*** *&* ***(b)*** *display the topography and gravity kernels (see expressions B7 and B13) for both an isostatic mantle and a (dynamic) viscous, compressible, self-gravity mantle. The viscous-flow kernels were calculated using a radial viscosity profile, derived by Mitrovica & Forte (2004) referred to as the 'V1' viscosity profile (Forte et al. 2010). Both free-slip and no-slip surface boundary conditions were employed to calculate the viscous-flow kernels.* ***(c)*** *&* ***(d)*** *display the amplitude spectra of both the isostatic topography and gravity predictions, respectively, that use shallow-mantle density anomalies extracted from the (Lu, Forte et al. 2020) tomography model. Shallow layers that are 200 and 400km thick are considered here. The predictions are compared to the amplitude spectra of the FR2021 topography data (Fig. 7, main text) and the GRACE gravity data.* ***(e)*** *&* ***(f)*** *display the spatial correlation, at each degree, of the predicted isostatic topography and gravity fields with the corresponding data: FR2021 and GRACE, respectively (panel c &d). Degree correlations and their significance levels are defined in O'Connell (1971).*

Additional references cited in Appendices:

Forte, A. M., & Peltier, W. R. (1987). Plate tectonics and aspherical Earth structure: The importance of poloidal-toroidal coupling. *Journal of Geophysical Research: Solid Earth*, **92**(B5), 3645-3679.

Gassmöller, R., Dannberg, J., Bangerth, W., Heister, T., & Myhill, R. (2020). On formulations of compressible mantle convection. *Geophysical Journal International*, **221**(2), 1264-1280.

Haxby, W. F., & Turcotte, D. L. (1978). On isostatic geoid anomalies. *Journal of Geophysical Research: Solid Earth*, **83**(B11), 5473-5478.

Heister, T., Dannberg, J., Gassmöller, R., & Bangerth, W. (2017). High accuracy mantle convection simulation through modern numerical methods–II: realistic models and problems. *Geophysical Journal International*, **210**(2), 833-851.

Jeffreys, H. (1929). *The Earth: Its Origin, History and Physical Constitution*. 2nd edition (Cambridge University Press), pp. 346.

Kronbichler, M., Heister, T., & Bangerth, W. (2012). High accuracy mantle convection simulation through modern numerical methods. *Geophysical Journal International*, **191**(1), 12-29.

Malvern, L. E. (1969). *Introduction to the Mechanics of a Continuous Medium*. (Prentice-Hall Inc.), pp. 713.

O'Connell, R. J. (1971). Pleistocene glaciation and the viscosity of the lower mantle. *Geophysical J. R. astr. Soc.*, **23**(3), 299-327.

Zhong, S., McNamara, A., Tan, E., Moresi, L., & Gurnis, M. (2008). A benchmark study on mantle convection in a 3-D spherical shell using CitcomS. *Geochemistry, Geophysics, Geosystems*, **9**(10).